nNOS-expressing interneurons control basal and behaviorally evoked arterial dilation in somatosensory cortex of mice

Christina T Echagarruga[1], Kyle W Gheres[2], Jordan N Norwood[3], Patrick J Drew[1,2,3,4]*

[1]Bioengineering Graduate Program, Pennsylvania State University, University Park, United States; [2]Molecular, Cellular, and Integrative Biology Graduate Program, Pennsylvania State University, University Park, United States; [3]Cell and Developmental Biology Graduate Program, Pennsylvania State University, University Park, United States; [4]Departments of Engineering Science and Mechanics, Biomedical Engineering, and Neurosurgery, Pennsylvania State University, University Park, United States

Abstract Cortical neural activity is coupled to local arterial diameter and blood flow. However, which neurons control the dynamics of cerebral arteries is not well understood. We dissected the cellular mechanisms controlling the basal diameter and evoked dilation in cortical arteries in awake, head-fixed mice. Locomotion drove robust arterial dilation, increases in gamma band power in the local field potential (LFP), and increases calcium signals in pyramidal and neuronal nitric oxide synthase (nNOS)-expressing neurons. Chemogenetic or pharmacological modulation of overall neural activity up or down caused corresponding increases or decreases in basal arterial diameter. Modulation of pyramidal neuron activity alone had little effect on basal or evoked arterial dilation, despite pronounced changes in the LFP. Modulation of the activity of nNOS-expressing neurons drove changes in the basal and evoked arterial diameter without corresponding changes in population neural activity.

*For correspondence: PJD17@PSU.EDU

Introduction

Understanding the mechanisms by which neural activity regulates local blood flow is a fundamental issue in neuroscience. Changes in neural activity are coupled to hemodynamics via neurovascular coupling, where neural activity drives the dilation of arterioles and other vessels (*Drew et al., 2011*; *Hillman, 2014*; *Hill et al., 2015*; *Mishra et al., 2016*; *Iadecola, 2017*; *Rungta et al., 2018*; *Drew, 2019*). Arterial dilations are most strongly correlated to increases in the gamma-band power of the LFP (local field potential), with lower correlation to the power in other bands of the LFP (*Goense and Logothetis, 2008*; *Logothetis, 2008*; *Mateo et al., 2017*; *Winder et al., 2017*; *Drew et al., 2020*). While it is controversial whether capillaries dilate (*Hall et al., 2014*; *Hill et al., 2015*; *Mishra et al., 2016*; *Rungta et al., 2018*) and whether this dilation is active or passive (*Mishra et al., 2016*; *Rungta et al., 2018*), sensory stimulation drives reliable and large (~20%) dilations of cerebral arteries in un-anesthetized animals (*Drew et al., 2011*; *Hill et al., 2015*; *Rungta et al., 2018*; *Drew, 2019*), which contributes to increases in blood flow. The sensory-evoked dilation initiates in the deeper layers of the cortex (*Tian et al., 2010*; *Rungta et al., 2018*), and rapidly propagates up to the surface (pial) arteries (*Drew et al., 2011*; *Mateo et al., 2017*) via conduction of an electrical signal (*Chen et al., 2011*; *Hillman, 2014*; *Longden et al., 2017*). Pial arteries show dilations correlated with spontaneous gamma band power (*Mateo et al., 2017*), and in awake animals, pial arteries show stimulus-selective dilations in response to sensory stimulation

(*Drew et al., 2011*; *Gao and Drew, 2016*; *Winder et al., 2017*). Pial arteries in the histologically reconstructed forelimb/hindlimb representation of primary somatosensory cortex dilate substantially more during locomotion than arteries just outside of this representation (*Gao et al., 2015*), although there may be less sensory specificity of the pial vessels responses in anesthetized animals (*O'Herron et al., 2016*). Simulations have suggested that the dilation of these arteries can play an important role increasing blood flow during functional hyperemia (*Schmid et al., 2017*; *Rungta et al., 2018*).

There are multiple signaling pathways and molecules implicated in linking neural activity (both directly and indirectly) to arteriole dilations (*Attwell et al., 2010*; *Cauli and Hamel, 2010*; *Kleinfeld et al., 2011*; *Lacroix et al., 2015*; *Longden et al., 2017*). While no single mechanism likely underlies neurovascular coupling, there is an extensive literature connecting the vasodilator nitric oxide (NO) to vasodilation both in the periphery and the brain (*Tanaka et al., 1991*; *Iadecola, 1992*; *Adachi et al., 1994*; *Stefanovic et al., 2007*; *Hosford and Gourine, 2019*; *Han et al., 2019a*). Recent in vitro evidence indicates neuronally-generated nitric oxide acts directly on arteries, while astrocytic signals control capillary dilations (*Mishra et al., 2016*). However, which set(s) of neurons control arterial diameter is not well understood. Optogenetic stimulation of interneurons drives a larger vasodilation than optogenetic stimulation of pyramidal neurons (*Vazquez et al., 2014*; *Anenberg et al., 2015*; *Uhlirova et al., 2016b*; *Vazquez et al., 2018*; *Krawchuk et al., 2020*), suggesting a subset of neurons exerts a disproportionate control over vasodilation. Optogenetic stimulation of neuronal nitric oxide (nNOS, also known as NOS1) expressing interneuron, but not in VIP or parvalbumin interneurons, produces increase in blood flow and vasodilation (*Krawchuk et al., 2020*; *Lee et al., 2020*), and this vasodilation is not accompanied by a detectable increase in neural activity (*Lee et al., 2020*), suggesting that nNOS neurons can influence local hemodynamics without detectably altering the activity of the rest of the network.

There are two types of nNOS–expressing neurons in the cortex, Type 1 and Type 2 (*Kawaguchi and Kubota, 1997*; *Vruwink et al., 2001*; *Kubota et al., 2011*). Type 1 nNOS neurons are sparse, are primarily found in deeper layers and express nNOS at higher levels. While Type 1 nNOS neurons receive many different neuromodulatory inputs (*Williams et al., 2019*; *Williams et al., 2018*), nearly all of them express the Substance P (SP) receptor (NK1R), and both single-cell genomic and histological studies have shown that they are the only cells in the mouse cortex that express the Substance P receptor (*Vruwink et al., 2001*; *Dittrich et al., 2012*; *Barbaresi et al., 2015*; *Endo et al., 2016*; *Tasic et al., 2016*). In vitro studies have shown that application of Substance P causes prolonged high-frequency spiking in type 1 nNOS neurons (*Dittrich et al., 2012*; *Endo et al., 2016*). Type 1 nNOS neurons also have extensive, long-range projecting axonal arbors that well-position them to influence the vasculature. In contrast, type 2 nNOS neurons are a heterogeneous group of interneurons that are substantially more numerous, found primarily in the deep and superficial layers of the cortex, with processes that can span multiple layers (*Perrenoud et al., 2012*). Type 2 nNOS neuron express nNOS at lower levels than type 1 nNOS neurons. The synthesis of NO by nNOS is calcium dependent, and as NOS is found both in the cell bodies and the processes of neurons NO will be produced throughout the cell when calcium levels rise with activity (*Valtschanoff et al., 1993*; *Blottner et al., 1995*).

While most studies of neurovascular coupling have focused on the impact of brief elevations of neural activity on hemodynamic signals, the role of neural activity in setting the baseline levels of these signals is not well understood, but have important implications for understanding the relationship between neural activity and hemodynamic signals. Most hemodynamic imaging modalities, such as BOLD fMRI, laser speckle, laser Doppler and Doppler ultrasound, are ratiometric, meaning they measure a percentage change from a baseline rather than an absolute change. This means that these measurements are sensitive to the baseline level of flow and dilation. For a given absolute change in flow, an elevated baseline will reduce the amplitude of the signal. This issue has long been appreciated in fMRI (*Cohen et al., 2002*; *Whittaker et al., 2016*; *Kim et al., 2020*), and there are techniques available to calibrate these signals (*Kim and Ogawa, 2012*). Differences in baseline are an important confound in comparisons across different groups, confounding aging and disease studies in humans (*D'Esposito et al., 2003*), particularly as in humans baseline blood flow drops with aging (*Ruitenberg et al., 2005*; *Wolters et al., 2017*). However, the impact of shifting the baseline levels, and particularly how neural activity could affect them, has been underappreciated in neurovascular coupling studies, which often compare the impact of disrupting a pathway in different

groups of animals using ratiometric techniques. This is particularly a problem because it is not well understood how baseline (non-stimulus evoked) levels of neural activity control blood flow, and ongoing neural activity in the un-anesthetized brain is very high. In contrast, two-photon imaging can measure absolute hemodynamic signals (*Shih et al., 2012b*), such as dilations of single vessels and velocities (*Kleinfeld et al., 1998*) and fluxes (*Chaigneau et al., 2003*; *Shih et al., 2009a*) of red blood cells.

Elucidating which neuronal cell types control arterial dilation (*Kleinfeld et al., 2011*; *Uhlirova et al., 2016a*) is important for interpreting hemodynamic imaging signals (*Logothetis, 2008*; *Kim and Ogawa, 2012*). Moreover, the regulation of *basal* arterial diameter, which plays a role in the control of baseline blood flow (*Gagnon et al., 2015*; *Schmid et al., 2017*), is also important because decreases in basal cerebral blood flow occur with aging, and the magnitude of these decreases predicts neurodegeneration (*Ruitenberg et al., 2005*; *Wolters et al., 2017*).

Results

We used two-photon microscopy (*Shih et al., 2012b*) to chronically image pial and penetrating arterioles in the somatosensory cortex of awake, head-fixed mice (*Figure 1A and B*; *Drew et al., 2011*; *Gao and Drew, 2016*; *Winder et al., 2017*) through polished and reinforced thinned-skull (PoRTs) windows (*Drew et al., 2010b*), which allow chronic imaging without inflammation. Because we were able to repeatedly image from the same vessels over multiple imaging sessions (*Figure 1C*), we were able to make quantitative comparisons of individual vessel diameter changes in response to manipulations of neural activity, rather than compare vessel responses from two different groups of animals. All drug/CNO, vehicle infusions, and injections were randomly counterbalanced across animals. As we measured from multiple vessels in each mouse, we used linear mixed-effect models (LME, see Materials and methods) (*Aarts et al., 2014*) for statistical tests to account for within-animal correlations (*Winder et al., 2017*; *Adams et al., 2018*) that make methods such as ANOVA inappropriate (*Aarts et al., 2014*).

We measured arteriole diameter dynamics evoked by locomotion, as behavior is the primary driver of neural and hemodynamic signals in the awake brain (*Figure 1D*; *Gao and Drew, 2016*; *Winder et al., 2017*; *Stringer et al., 2019*), and because sensory stimulation in awake animals invariably elicits movement (*Cooke et al., 2015*; *Drew et al., 2019*; *Musall et al., 2019*; *Salkoff et al., 2020*). The change in diameter and neural activity during locomotion was quantified by averaging the dilation or neural activity 3 to 4 s after the onset of locomotion. We reconstructed the locations of individual arterioles relative to the forelimb/hindlimb (FH/HL) representation in somatosensory cortex (purple and green shaded regions *Figure 1B*, top), as arteries inside the FL/HL region dilate selectively in response to locomotion, significantly more so than arteries immediately outside the histologically-identified FL/HL (*Gao et al., 2015*). Locomotion-induced arterial dilations in the FL/HL area of somatosensory cortex have highly reliable and stereotyped dynamics (*Huo et al., 2015b*), and are unaffected by pharmacological manipulations of heart rate and blood pressure (*Huo et al., 2015a*), consistent with local neural control. During bouts of voluntary locomotion, neural activity increased substantially in the forelimb/hindlimb representation in somatosensory cortex, as measured by changes in multi-unit firing rate and power in the gamma-band of the LFP (*Figure 1—figure supplement 1*; *Huo et al., 2014*; *Zhang et al., 2019*). These increases are driven primarily by cutaneous sensation rather than proprioception (*Chapin et al., 1981*; *Chapin and Woodward, 1981*; *Chapin and Woodward, 1982*; *Chapin and Lin, 1984*). During locomotion, this neural activity is sustained, and shows minimal adaptation (*Zhang et al., 2019*). In response to this increase in neural activity, both pial and penetrating arterioles in the FL/HL representation dilated (*Huo et al., 2015b*; *Gao and Drew, 2016*; *Figure 1D* and *Figure 1—figure supplement 2* and *Video 1* and *2*) with short latency (onset time: 0.59 ± 0.31 s in the FL/HL region).

Basal arterial diameter and evoked dilation are controlled by local neural activity

We first determined the role of overall local neural activity in maintaining baseline arterial diameter. We refer to the diameter of the vessel during periods lacking locomotion (see Materials and methods) as the 'basal' diameter. We suppressed the activity of all neurons via intracranial infusions of muscimol (a GABA$_A$ receptor agonist) and compared the changes in neural activity and arterial
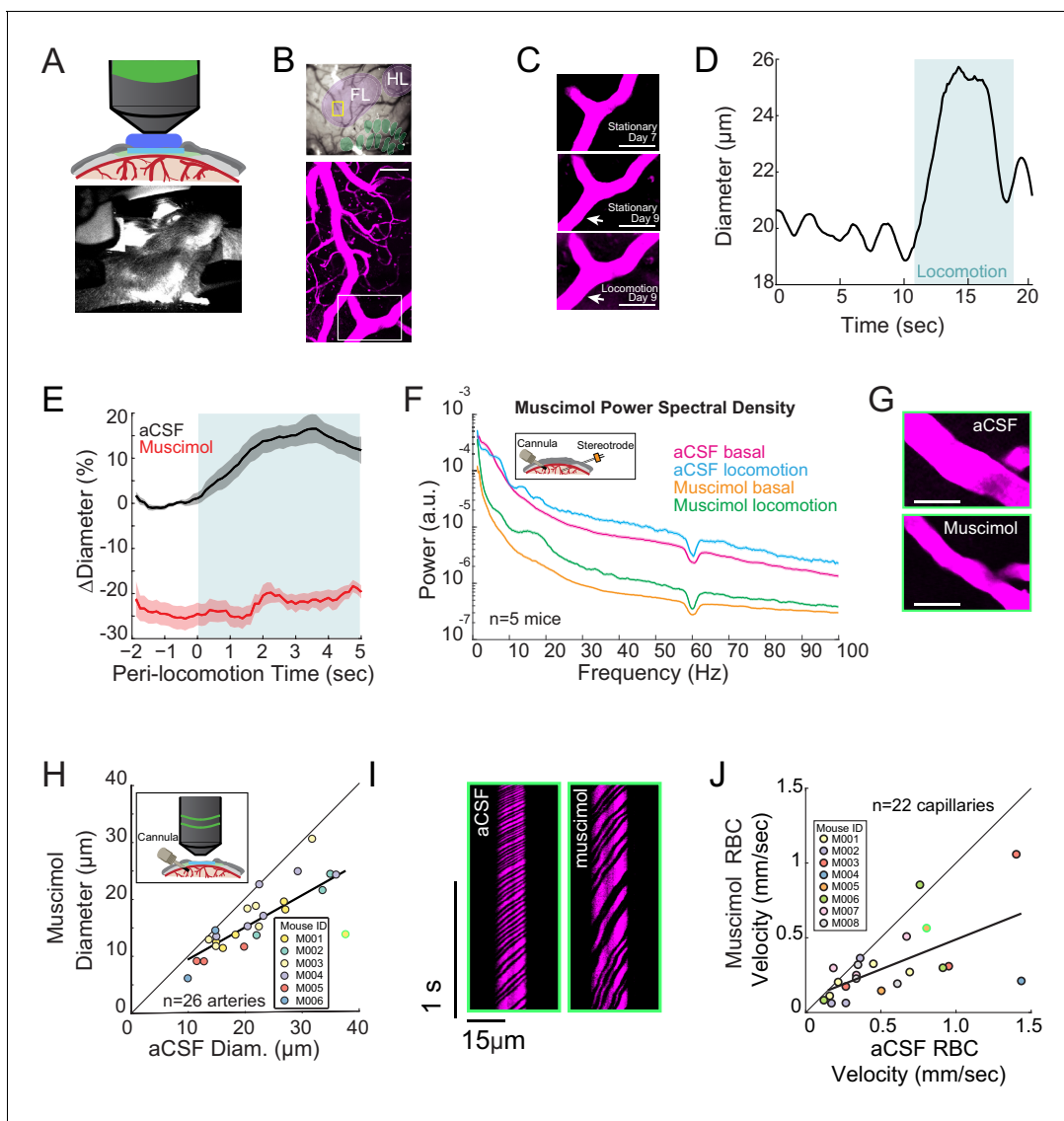
Figure 1. Local neural activity controls basal and evoked arteriole diameter. (**A**) Top, schematic of imaging window. Bottom, photo of mouse on spherical treadmill. (**B**) Top, photo of the pial vasculature of the somatosensory cortex through the PoRTs window. Cytochrome oxidase staining localized the forelimb/hindlimb (FL/HL, purple) and vibrissae cortex (green). Bottom, a maximum projection of two-photon images of vasculature within the yellow box in the top image. Scale bar 50 μm. (**C**) Top and middle, two-photon images (from white box in B, bottom) of the same arteriole 7 and 9 days after window implantation, both from stationary periods. Bottom, arteriole 9 days after implantation during locomotion. Scale bar 50 μm. (**D**) Locomotion induces rapid dilation in pial arterioles. Diameter (from region marked by white arrow in **C**) plotted versus time for a single locomotion event. Blue shading denotes period of locomotion. (**E**) Population locomotion-triggered averages following aCSF and muscimol infusions for arterioles ≤ 25 μm in basal diameter. For both cases, the individual diameters are normalized by the average basal diameter of the vessel after vehicle infusion. Note the rapid rise to peak in the control, and the lack of dilation in muscimol-infused mice, showing the locomotion-triggered response is under local neural control. Shading represents mean ± standard error. (**F**) LFP power spectra during stationary periods (basal) and locomotion after muscimol infusion, normalized to vehicle infusion in the same animal. Shading represents mean ± standard error. (**G**) Representative images of a pial arteriole during periods of no locomotion after vehicle infusion (top) and after muscimol infusion (bottom). Scale bar 50 μm. (**H**) Basal arteriole diameter following vehicle infusion plotted versus basal diameter after muscimol infusion. Each point is a single vessel, and the mouse identity is represented by the color. The black line shows the linear regression of aCSF vs. muscimol diameter. The point outlined in green is representative image from G. (**I**) Representative space-time image of linescans of the same capillary after aCSF or muscimol infusion. (**J**) Basal red blood cell (RBC) velocity plotted after vehicle infusion (x-axis) vs. after muscimol infusion (y-axis). The point outlined in green is the vessel shown in **I**.

The online version of this article includes the following figure supplement(s) for figure 1:

Figure supplement 1. Example neural responses in forelimb/hindlimb representation of somatosensory cortex during voluntary locomotion.

Figure supplement 2. Diameter changes in penetrating arterioles.

Figure supplement 3. Muscimol infusion did not significantly affect capillary diameter.

Figure 1 continued on next page

Figure supplement 4. Muscimol infusion did not significantly affect basal arteriole diameter variance.

Figure supplement 5. Effects of chemogenetic and pharmacological manipulation on locomotion behavior.

diameter dynamics to artificial cerebrospinal fluid (aCSF- a vehicle control) infusions in the same mouse. Infusions of muscimol substantially decrease (by 70–95%) neural activity ~1.5 mm from the cannula (*Winder et al., 2017*; *Zhang et al., 2019*), and so will suppress activity in all cortical layers, unlike topical administration of drugs which typically only affect the superficial layers (*Ferezou et al., 2006*). Control experiments have shown that cannula implantations do not alter hemodynamic responses (*Winder et al., 2017*). To visualize any change in vessel diameter across all the measured vessels we made a scatter plot of vessel diameters (*Figure 1G–H*), with the abscissa the diameter measured after the control (vehicle) infusion, and the ordinate the diameter after the drug infusion (muscimol in this case). If there is no effect of the drug, the points will be scattered along the unity line. If the drug causes constriction or dilation, the points will be respectively above or below the line. We found that after the infusion of muscimol, there was a substantial decrease in baseline and locomotion-evoked gamma-band power relative to within animal aCSF controls (*Figure 1F*, basal $-75.2 \pm 7.1\%$, $p<3.0\times10^{-4}$; locomotion, $-77.0 \pm 6.6\%$, $p<2.0\times10^{-4}$). We found that muscimol infusions led to a substantial decrease in the basal arteriole diameter (*Figure 1G–H*, $-25.4 \pm 2.3\%$, LME $p<2.8\times10^{-4}$, n = 6 mice, 26 arterioles; *Figure 1—figure supplement 2B*). The effects of muscimol infusions were not due to direct actions on the cerebral vasculature, as multiple large-scale single-cell sequencing studies have shown that mice lack GABA receptors on endothelial cells (*Sabbagh et al., 2018*; *Vanlandewijck et al., 2018*; *Zeisel et al., 2018*) and physiological experiments using optogenetic stimulation of interneurons with and without GABA-receptor blockade have shown there is no impact of blocking GABAergic signaling on vessel dilation (*Anenberg et al., 2015*; *Vazquez et al., 2018*). Rather than being driven by direct action of muscimol on the vasculature, this constriction is likely due to the removal of tonic vasodilatory signals released by neurons.

To determine if this decrease in basal arteriole diameter drove a decrease in blood flow, we then measured red blood cell (RBC) velocity in the capillaries (*Kleinfeld et al., 1998*; *Chaigneau et al., 2003*; *Drew et al., 2010a*). Capillary RBC velocity was markedly decreased in muscimol-infused mice relative to aCSF infusions (*Figure 1I and J*, $-34.5 \pm 27\%$, LME $p<1.5\times10^{-3}$, n = 8 mice, 22 capillaries). We observed no significant change in the diameter of the capillaries following the infusion of muscimol (aCSF-muscimol difference: 0.03 ± 0.85 µm, LME $p<0.94$, *Figure 1—figure supplement 3A and B*). Suppressing neural activity with muscimol did not abolish spontaneous fluctuations in arteriole diameter (*Figure 1—figure supplements 4A*, -14.2±67%, LME $p<0.06$, n = 6 mice, 26 vessels), consistent with previous reports of vessel-autonomous oscillations in arterioles (*Winder et al., 2017*). Taken together, these results suggest that baseline levels of neural activity have a tonic vasodilatory effect on cerebral arterioles (either directly, or through astrocytes), and decreasing neural activity causes a corresponding decrease in arteriole diameter and blood flow.

We then examined the role of neural activity in locomotion-evoked dilations. We calculated locomotion-triggered averages using only the arterioles histologically identified to be in the FL/HL region (using cytochrome oxidase staining [*Adams et al., 2018*]), as vessels outside this region are less responsive to locomotion (*Gao et al., 2015*). We also restricted this locomotion-triggered analysis to arterioles < 25 microns in diameter, as arterial reactivity decreases with increasing arteriole size (*Lee et al., 2001*; *Drew et al., 2011*; *Gao et al., 2015*), so larger vessels tend to be less
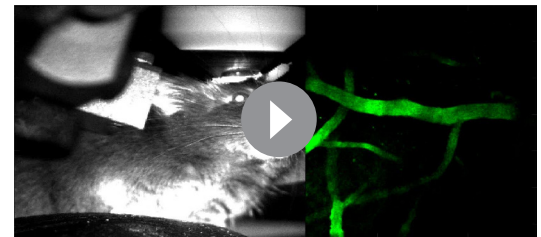
Video 1. Locomotion produces a rapid dilation in pial arterioles. This movie shows in vivo imaging of a surface arteriole diameter in the somatosensory cortex through the PoRTs window using two-photon microscopy. Left, behavioral camera. Right, FITC-filled arteriole diameter (region marked by white arrow) was plotted versus time in green.

https://elifesciences.org/articles/60533#video1
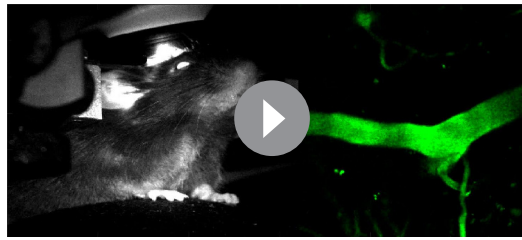
Video 2. Locomotion produces a rapid dilation in pial arterioles. This movie shows in vivo imaging of a surface arteriole diameter in the somatosensory cortex through the PoRTs window using two-photon microscopy. Left, behavioral camera. Right, FITC-filled arteriole diameter (region marked by white arrow) was plotted versus time in green.
https://elifesciences.org/articles/60533#video2

responsive to changes in neural activity than smaller vessels. We found that the locomotion-evoked dilation of these arterioles was blocked by local silencing of neurons with muscimol (*Figure 1E* locomotion-evoked dilation: aCSF 15.8 ± 2.7%; muscimol −21.6 ± 1.9%, LME p<5.2×10^{-6}, n = 6 mice, 12 arterioles in FL/HL representation), suggesting that these arteriole dilations were not due to non-specific cardiovascular responses (*Huo et al., 2015a*) or modulatory input from other brain regions directly onto the vessels (*Drew et al., 2008*), but rather controlled by local activity. Similar effects were observed in penetrating arterioles (*Figure 1—figure supplement 2B and C*; see also *Figure 6—figure supplement 2*). Note that the locomotion-evoked numbers reporte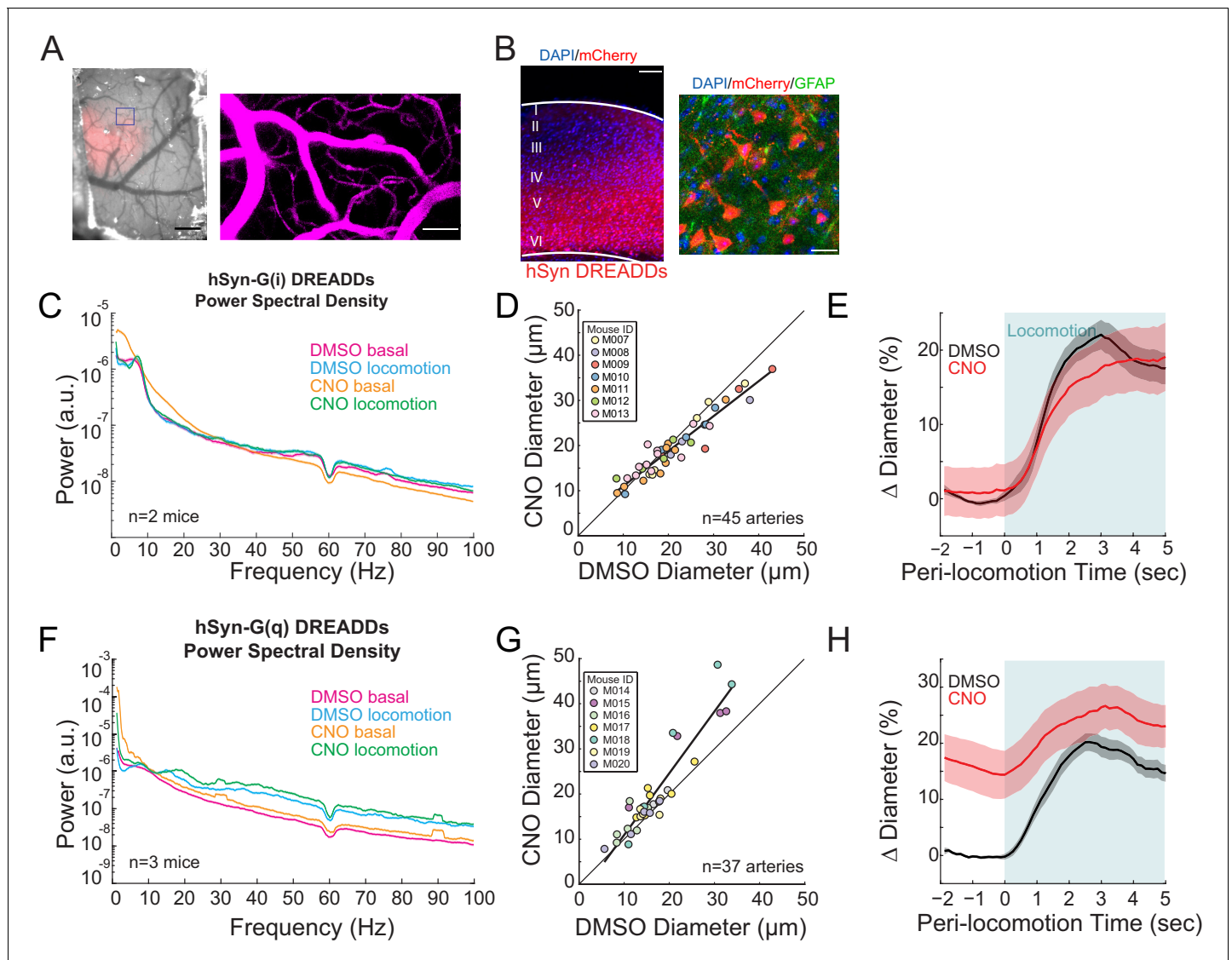d in the text (unless otherwise stated), are relative to the control baseline, and thus include both the effects of the manipulation on the basal diameter and the evoked diameter. We split out the effects of our manipulations on the locomotion-evoked response in the analysis in *Figure 6—figure supplement 2*. For comparison of the results obtained with these two approaches, during muscimol infusions, there was a small locomotion-evoked increase from the pre-locomotion baseline (15.37 ± 8.11% vs. 5.14±11.09%, LME p<0.001, n = 5 animals, 12 vessels) (*Figure 6—figure supplement 2*). Infusions of muscimol and other manipulations of neural activity did not cause significant differences in the amount of locomotion relative to controls, indicating that behavior is not an origin of this difference (*Figure 1—figure supplement 5*), and consistent with previous work showing that pharmacological silencing of motor cortex disrupted complex movements, but not locomotion (*Beloozerova and Sirota, 1993*). Thus, both basal diameter and sensory-evoked arterial dilations in the FL/HL region of somatosensory cortex are under control of local neural activity.

Bidirectional chemogenetic manipulation of local neural activity controls basal arterial diameter

We then asked if we could bi-directionally manipulate arterial diameters using chemogenetic techniques to drive changes in overall neural activity. We expressed either hM4D-G(i) or hM3D-G(q)-coupled DREADDs (*Urban and Roth, 2015*) pan-neuronally under a human synapsin promoter (hSyn) in C57BL/6J mice. G(i)- and G(q)-coupled DREADDs will respectively decrease and increase the excitability of the cells expressing them after injection of the DREADDs agonist CNO. As a control, mice infected with an AAV encoding only the fluorescent reporter mCherry did not show significant changes in neural activity, or in basal or evoked arterial diameter after the injection of CNO (*Figure 2—figure supplement 1B–D*), showing CNO has minimal off-target effects on neural activity and arterial diameters.

We imaged arterioles in the DREADD-expressing region of cortex (identified by mCherry expression seen in vivo, *Figure 2A*, and histologically, *Figure 2B*). Injections of CNO in mice with pan-neuronal expression of hM4D-G(i) DREADDs resulted in a non-significant decrease in gamma-band power relative to vehicle injections (*Figure 2C*, basal −1.9 ± 27.2%, p<0.09; locomotion, +3.6 ± 10.3%, p<0.07), likely because of the parallel changes in excitability of inhibitory and excitatory cells cancelled out. Still, activation of hM4D-G(i) DREADDs resulted in significant decreases in basal arterial diameter (*Figure 2D*, −7.1 ± 7.0%, LME p<0.02 n = 7 mice, 45 vessels), which was particularly noticeable in the largest arterioles. We note that the hM4D-G(i) DREADDs did not uniformly lower neural activity, as we observed bursting activity in our electrophysiological recordings every few seconds (*Figure 2—figure supplement 2A*), and corresponding arterial dilations at similar frequencies (*Figure 2—figure supplement 2B*). While we saw clear constrictions in arteriole diameters when activating hSyn G(i)-DREADDs relative to baseline, there were also large spontaneous dilations, which on average cancelled out. The net effect of hM4D-G(i) DREADDs on the locomotion-evoked

Figure 2. Neural activity bidirectionally controls basal arteriole diameter. (A) Left, image through the polished and reinforced thinned-skull window showing AAV expression (red) in the somatosensory cortex (scale bar 1 mm). Right, vasculature within box of A. (B) Representative image of AAV-hSYN-HA-hM3D(Gq)-mCherry expressing cortex. Left is wide field image of hSyn-mCherry DREADDs virus (red) in cortex with DAPI (blue) staining (scale bar 100 μm). Right is magnified image of hSyn-mCherry DREADDs virus (red) in cortex with DAPI (blue) and GFAP (green) staining (scale bar 30 μm), showing the virus was not expressed in astrocytes. Data in (C–E) are from mice injected with AAV-hSYN-HA-hM4D(Gi)-mCherry, data in (F–H) is from mice injected with AAV-hSYN-HA-hM3D(Gq)-mCherry. (C) LFP power spectra during stationary periods (basal) and locomotion after CNO injection in hSyn G(i) DREADDs mice, normalized to stationary periods during vehicle injection in the same animal. (D) Plot of basal arteriole diameter after vehicle injection (x-axis) versus CNO injection (y-axis). (E) Population locomotion-triggered averages for vessels ≤ 25 μm in diameter after vehicle and CNO injections. (F) LFP power spectra during stationary periods (basal) and locomotion after CNO injection in hSyn G(q) DREADDs mice, normalized to stationary periods during vehicle injection of the same mouse. (G) Plot of basal arteriole diameter after vehicle injection (x-axis) versus CNO injection (y-axis). (H) Population locomotion-triggered averages in response to locomotion after vehicle and CNO injections.

The online version of this article includes the following figure supplement(s) for figure 2:

Figure supplement 1. No significant effect of CNO on basal arteriole diameters or neural activity.

Figure supplement 2. hM4D-G(i) DREADDs cause bursts on neural activity.

response was minimal (*Figure 2E*, locomotion-evoked response: vehicle 20.5 ± 2.0%, CNO 18.3 ± 4.1%, LME p<1, n = 7 mice, 25 arterioles in FL/HL representation).

When we pan-neuronally expressed hM3D-G(q) DREADDs, which will increase excitability and intracellular calcium levels (*Alexander et al., 2009*; *Pati et al., 2019*), activation of the DREADDs

with CNO injections caused increases in gamma-band power relative to vehicle (*Figure 2F*, basal 18.6 ± 11.2%, p<0.02; locomotion, 43.6 ± 15.0%, p<7.1×10^{-3}). Injections of CNO caused substantial increases in the basal arterial diameter over controls (*Figure 2G*, +18.8 ± 5.6%, LME p<0.03, n = 7 mice, 37 vessels). The increase in basal arteriole diameter by hM3D-G(q) DREADD activation was comparable to the locomotion-evoked response (*Figure 2H*, locomotion-evoked response: vehicle 18.6 ± 1.7%, CNO 26.0 ± 4.2%, LME p<1, n = 7 mice, 23 arterioles in FL/HL representation). These results suggest that neurons, or a subset of neurons, tonically release vasodilator(s) due to ongoing background neural activity, and elevation of this activity can drive arterial dilations.

Altering pyramidal neuron excitability drives large neural activity changes without corresponding changes in arterial diameter

The importance of local neural activity on the regulation of arterial dilation raises the question of which sub-population(s) of neurons are involved. We manipulated the excitability of pyramidal neurons by injecting AAVs encoding hM3D(q) or hM4D(i) DREADDs under a CaMKIIa promoter, which will restrict the expression to pyramidal neurons (*López et al., 2016*; *Yuan and Grutzendler, 2016*). CaMKIIa-DREADDs labeled cells colocalized with CaMKIIa expression and were primarily localized to neurons with cell bodies in layer 5 (*Figure 3A*). Previous work has shown that optogenetic stimulation of layer 5 pyramidal neurons drives increases in neural activity in all layers via recurrent connections, and these increases in neural activity are very similar to what is seen with sensory stimulation (*Vazquez et al., 2014*; *Vazquez et al., 2018*), so chemogenetic stimulation of these cells will likely produce neural activity patters similar to those normally found in the cortex. The dilatory signal in the deeper cortical layers is electrically conducted through the vasculature rapidly by gap junctions (*Bagher and Segal, 2011*; *Welsh et al., 2018*) to the pial vessels (*Rungta et al., 2018*). Activating hM4D(i) DREADDs in excitatory neurons with CNO caused large decreases in basal gamma-band power (*Figure 3B and D*, basal −36.0 ± 16.4%, p<0.01; locomotion, −26.8 ± 15.8%, p<0.02). When hM3D(q) DREADD receptors in excitatory neurons were activated, a corresponding large increase in basal gamma-band power was observed (*Figure 3C and G*, basal +52.4 ± 18.9%, p<5.0×10^{-3}; locomotion, +50.9 ± 31.6%, p<0.02). Despite the large changes in neural activity, we did not see significant changes in the basal arterial diameters with manipulation of pyramidal neuron activity (−2.2 ± 5.7%, LME p<1, n = 7 mice, 38 arterioles for inhibition and +7.2 ± 8.8%, LME p<0.66, n = 6 mice, 41 arterioles for excitation) (*Figure 3E* and *Figure 3H*, respectively). The locomotion-evoked dilations were also not affected by manipulations of neural excitability (*Figure 3F* G(i) DREADDS: vehicle 25.3 ± 1.9%, CNO 21.6 ± 4.3%,LME p<1, n = 7 mice, 29 arterioles in FL/HL representation; *Figure 3I* G (q) DREADDS: vehicle 19.1 ± 2.3%, CNO 17.3 ± 4.7% LME p<1, n = 6 mice, 13 arterioles in FL/HL representation).

The lack of change in the arterial diameters could not be due to a lack of an effect of the chemogenetic manipulations as the changes in neural activity were very large. The decreases in basal neural activity generated by activation of G(i)-coupled DREADDs in pyramidal neurons were nearly as large as those elicited by muscimol (*Figure 3B*), and the increases in basal neural activity generated by activation of G(q)-coupled DREADDs in pyramidal neurons were as large as those seen during locomotion (*Figure 3C*), yet in neither of these cases did we observe arterial diameter changes of similar magnitude. Thus, pyramidal neuron activity is a strong driver of gamma band LFP power, but only has a moderate effect on basal arterial diameter, and little effect on the locomotion-evoked dilations.

nNOS-expressing neurons and NO signaling control arterial diameter independent of overall neural activity

Previous work has implicated neuronally-generated nitric oxide (NO) (*Hosford and Gourine, 2019*), generated by interneurons (*Krawchuk et al., 2020*; *Lee et al., 2020*) in the dilation of cerebral arteries. To test the role of neuronal nitric oxide synthase (nNOS) expressing neurons, we expressed hM3D(q) and hM4D(i) DREADDs along with the reporter protein mCherry in nNOS-expressing neurons using flexed AAVs in nNOS-cre- mice (B6.129-*Nos1*$^{tm1(cre)Mgmj}$/J, Jackson Laboratory #017526) (*Leshan et al., 2012*; *Augustine et al., 2018*). Expression of the reporter protein mCherry was primarily in the deeper and more superficial layers of the cortex (*Figure 4A,B*), consistent with the observed densities of nNOS-expressing neurons (*Perrenoud et al., 2012*). Co-labeling with
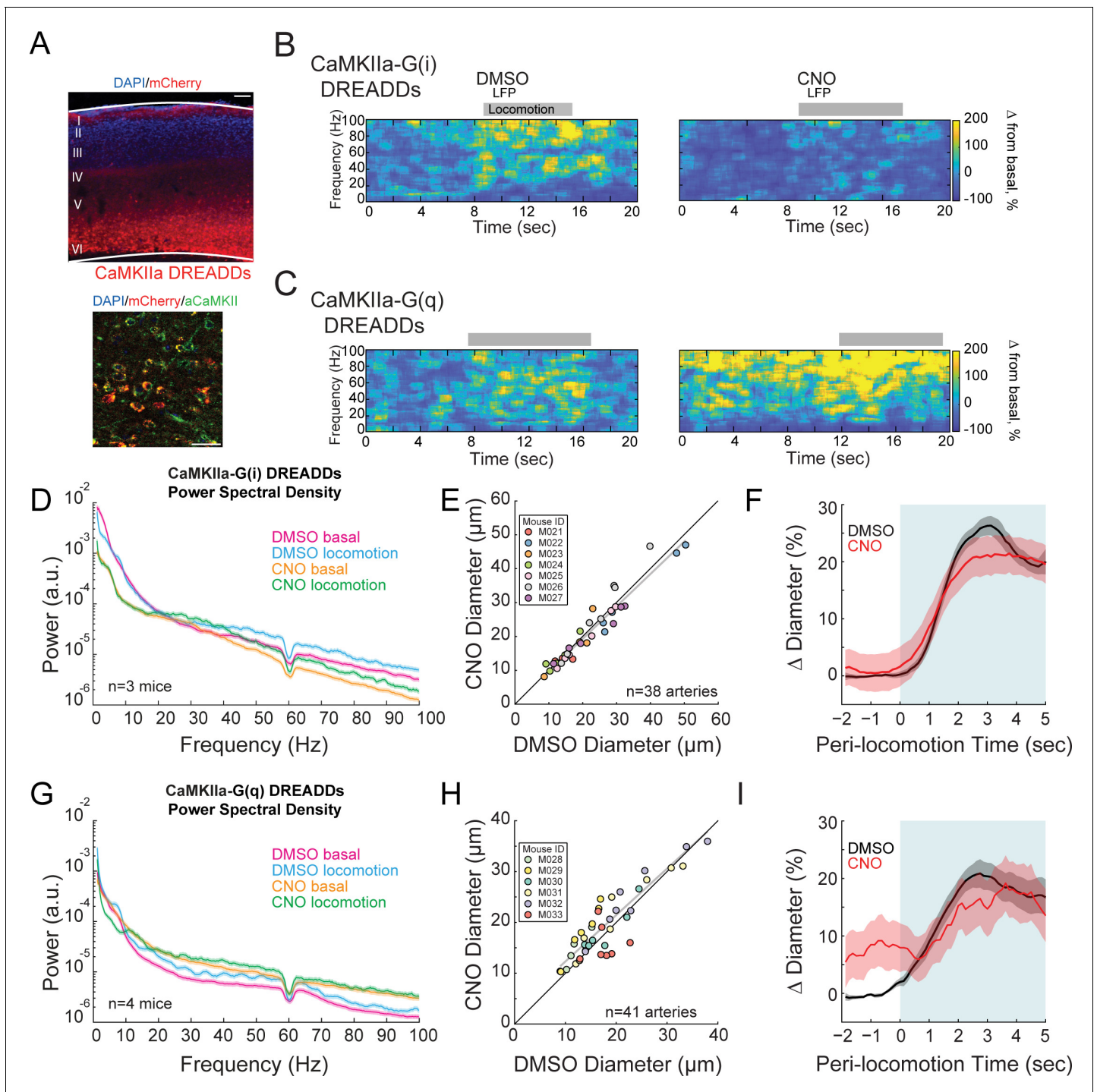
Figure 3. Activity, but not of pyramidal neurons, bidirectionally controls basal arteriole diameter. (**A**) Representative image of AAV-CaMKIIa-hM3D(Gq)-mCherry infected cortex, where DREADDs are expressed under a CaMKIIa promoter. Top image is wide field image of CaMKIIa-mCherry DREADDs virus (red) in cortex with DAPI (blue) staining. Scale bar 100 μm. Bottom is a magnified image of CaMKIIa-mCherry DREADDs (red) expressed in cortex with DAPI (blue) and αCaMKII (green) staining showing expression in excitatory neurons. Scale bar 30 μm. (**B**) Representative LFP spectrograms of CaMKIIa-G(i) DREADD expressing mouse after vehicle (left) or CNO (right) injection. Locomotion events are denoted by shading. (**C**) Representative LFP spectrograms of CaMKIIa-G(q) DREADD expressing mouse (expression in pyramidal neurons) after vehicle (left) or CNO (right) injection. Data in **D-F** are from mice injected with AAV-CaMKIIa-hM4D(Gi)-mCherry, data in **G-H** is from mice injected with AAV-CaMKIIa-hM4D(Gq)-mCherry (expression in pyramidal neurons). (**D**) LFP power spectra during stationary periods (basal) and locomotion after CNO injection in CaMKIIa G(i) DREADDs mice, normalized to stationary periods during vehicle injection of the same mouse. (**E**) Plot of basal arteriole diameter after vehicle injection (x-axis) versus CNO injection (y-axis). (**F**) Population locomotion-triggered averages after vehicle and CNO injections for arterioles ≤ 25 μm in basal diameter. (**G**) LFP

Figure 3 continued on next page

antibodies for nNOS (*Figure 4A,B*) showed co-expression (white) of mCherry (magenta) and nNOS (green) in both cell bodies and processes of neurons. Neurons showing strong anti-nNOS labeling were taken to be type 1 nNOS neurons, with-type 2 nNOS neurons showing less intense anti-nNOS labeling, consistent with previous anatomical studies (*Perrenoud et al., 2012*). Immunolabeling (n = 2 mice) revealed that 28.6% (2/7 cells) type 1% and 35.2% (19/54) of type 2 nNOS neurons expressed DREADDs, and that 44.6% (21/47) of DREADD-expressing cells were nNOS positive. Neurons expressing mCherry also expressed GAD65, indicating they were GABAergic interneurons (*Figure 4C*).

CNO injections in mice expressing G(i)-DREADD in nNOS-expressing neurons resulted in no significant change in gamma-band power (*Figure 4D*, basal $-1.2 \pm 11.6\%$, p<1; locomotion, $-5.7 \pm 2.2\%$, p<0.09). Increasing the excitability of nNOS-expressing neurons resulted in a significant decrease in basal gamma-band power (*Figure 4G*, basal $-19.8 \pm 2.6\%$, p<4.0×10^{-3}; locomotion, $-12.8 \pm 4.7\%$, p<0.10), consistent with these neurons being inhibitory. However, decreasing the excitability of nNOS neurons drove substantial and significant decreases in both basal arteriole diameter ($-10.3 \pm 6.4\%$ LME p<1.3×10^{-4}, n = 9 mice, 49 vessels *Figure 4E*) and the locomotion-induced dilation (*Figure 4F*, vehicle $15.3 \pm 2.0\%$, CNO $0.3 \pm 4.3\%$, LME p<6.3×10^{-3}, n = 6 mice, 22 arterioles in FL/HL representation). Elevating the excitability of nNOS-expressing neurons significantly increased the basal arterial diameter ($+5.8 \pm 6.6\%$, LME p<2.7×10^{-4}, n = 8 mice, 52 vessels, *Figure 4H*), but did not increase the locomotion-evoked increase above the control (*Figure 4I* vehicle $17.4 \pm 1.8\%$, CNO $19.6 \pm 3.8\%$, LME p<1, n = 8 mice, 25 arterioles in FL/HL representation). Interestingly, the diameter changes moved in the opposite direction as neural activity when the excitability of nNOS-expressing neurons was increased, consistent with nNOS neurons being inhibitory.

We then tested whether the effects of nNOS-expressing neuron activity on arteriole diameter was mediated by NO, as these neurons can also release vasoactive peptides (*Cauli et al., 2004*). Previous studies with NOS inhibitors have shown conflicting effects (*Lindauer et al., 1999*; *Stefanovic et al., 2007*). Discrepancy in the literature could be due to differences in experimental methodology: topical application of drugs may not reach lower cortical layers (*Greenberg et al., 1997*; *Ferezou et al., 2006*) where most of the highly expressing nNOS neurons reside, and systemic administration impacts the cardiovascular system. To avoid these experimental confounds, we infused the water-soluble NO synthase inhibitor, Nω-nitro-L-arginine methyl ester (L-NAME) through an implanted cannula to decrease NO-mediated signaling. In our hands, pharmacological infusions through cannula affect all cortical layers within ~1.5 mm of the infusion site (*Winder et al., 2017*). Note that recent studies, using both single-cell genomic methods as well as immunohistochemistry, have shown that some cortical neurons express eNOS (*Yousef et al., 2004*; *Lein et al., 2007*; *Tasic et al., 2016*), and that some endothelial cells of cerebral arterioles express nNOS (*Vanlandewijck et al., 2018*; *Zeisel et al., 2018*), so the endothelial/neural specificity of these enzymes is not complete. Additionally, crystal structures and careful pharmacology experiments have revealed that 'selective' pharmacological inhibitors of nNOS are much less selective than was originally thought (*Bland-Ward and Moore, 1995*; *Reiner and Zagvazdin, 1998*; *Engelhardt et al., 2006*; *Pigott et al., 2013*; *Poulos and Li, 2017*), so it is likely that there are no inhibitors of nNOS or eNOS are specific enough to target one enzyme over another in vivo. Finally, locomotion-evoked dilations are unlikely to be mediated by eNOS expressed in endothelial cells as increases in eNOS activity in response to flow-evoked changes in diameter evolve over minutes, not seconds (*Kim et al., 2016*) (too slow to account for the locomotion-evoked dilations), and there are no shear-stress changes seen with sensory-evoked dilation (*Ngai and Winn, 1996*). Blocking the production of NO caused no significant change in the basal gamma-band power (*Figure 4—figure supplement 1A*, basal $-5.0 \pm 8.5\%$, p<0.55; locomotion, $-7.5 \pm 9.6\%$, p<0.43), but drove a decrease in basal and locomotion-evoked arterial diameter ($-10.6 \pm 4.6\%$, LME p<7.6×10^{-6}, n = 6 mice, 36 arterioles, and vehicle $13.2 \pm 2.4\%$, L-NAME $4.2 \pm 3.8\%$, LME p<0.04, n = 6 mice, 20 arterioles in FL/HL representation, *Figure 4—*
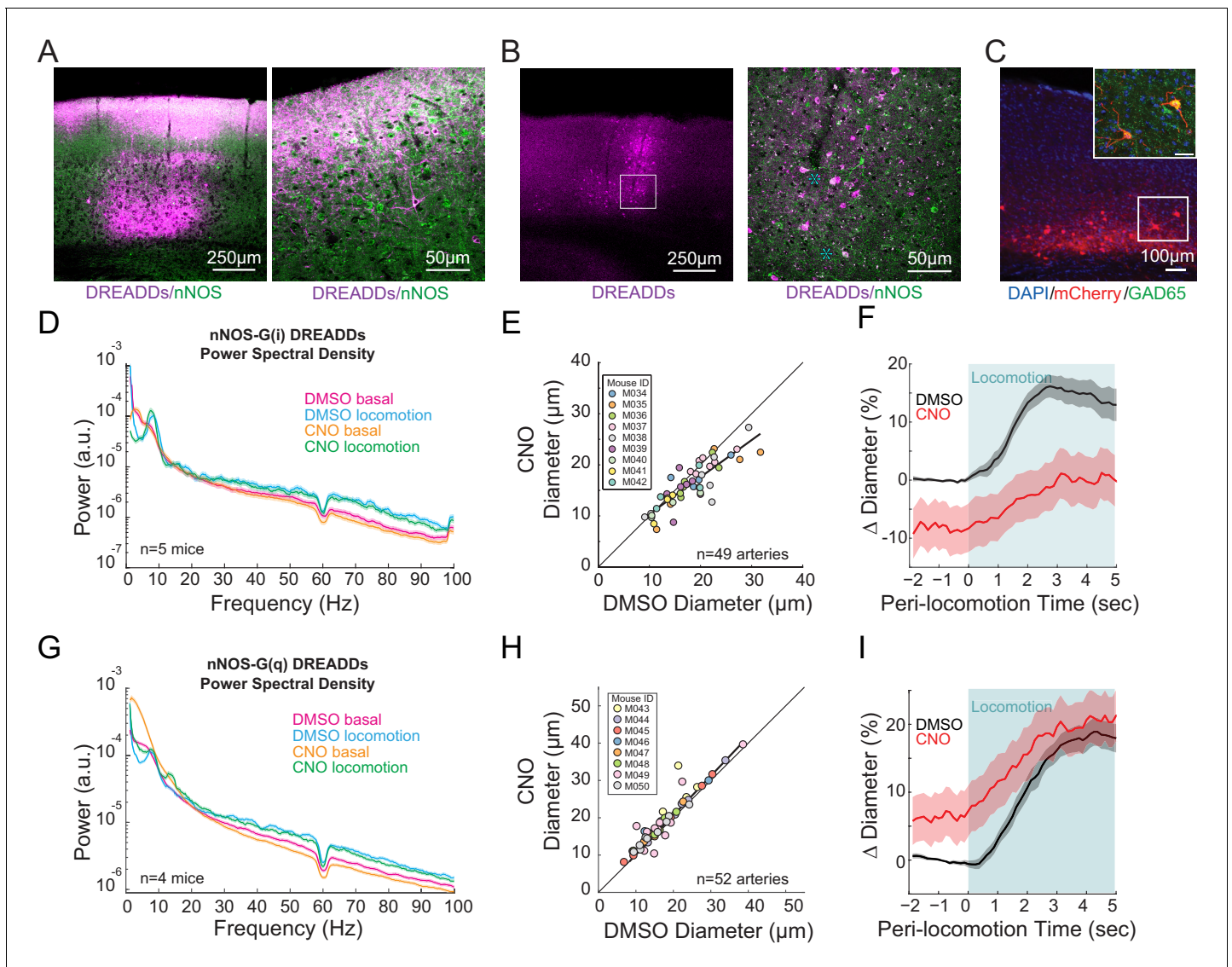
Figure 4. nNOS expressing neurons controls arteriole diameter independent of overall neural activity. (**A**) Representative image of cortex taken of AAV-hSyn-DIO-hM3D(Gq)-mCherry in nNOS-cre mice, where DREADDs expressed in nNOS+ cells. The mCherry label is magenta, nNOS antibody is green. Co-labeling in processes in cell bodies shows up as white. Blue asterixis denote putative type 1 nNOS neurons. Dark vertical streaks are blood vessels. (**B**) Left, wide-field image of DREADD-infected somatosensory cortex. Right, enlargement of area in the white box, showing expression around blood vessel. (**C**) Left image is wide-field image of nNOS-mCherry DREADDs expression (red) in cortex with DAPI (blue) staining. Scale bar 100 μm. Right image is zoomed image of nNOS-mCherry DREADDs virus (red) in cortex with DAPI (blue) and GAD65 (green) staining, Scale bar 30 μm. Data in **D-F** are from nNOS-cre mice injected with AAV-hSyn-DIO-hM4D(Gi)-mCherry, data in **G-I** is from nNOS-cre injected with AAV-hSyn-DIO-hM4D(Gq)-mCherry. (**D**) LFP power spectra during stationary periods (basal) and locomotion after CNO injection in nNOS G(i) DREADDs mice, normalized to vehicle injection of the same mouse. (**E**) Plot of basal arteriole diameter after vehicle injection (x-axis) versus CNO injection (y-axis). (**F**) Population locomotion-triggered diameter averages after vehicle and CNO injections for arterioles ≤ 25 μm in basal diameter. (**G**) LFP power spectra during stationary periods (basal) and locomotion after CNO injection in nNOS G(q) DREADDs mice. (**H**) Plot of basal arteriole diameter after vehicle injection (x-axis) versus CNO injection (y-axis). (**I**) Population locomotion-triggered averages after vehicle and CNO injections for arterioles ≤ 25 μm in basal diameter.

The online version of this article includes the following figure supplement(s) for figure 4:

Figure supplement 1. NO produced by nNOS expressing neurons controls arteriole diameter independent of overall neural activity.

figure supplement 1B and C). The basal arterial diameter constrictions produced by L-NAME were not significantly different from those produced by G(i) DREADDs in nNOS neurons (−10.6% vs. −10.3%, LME p<0.57 *Figure 4—figure supplement 1D*). Although there is likely some contribution from the inhibition of eNOS contributing to these constrictions (*Atochin and Huang, 2011*), these results are consistent with the hypothesis that the NO produced by nNOS-expressing neurons contributes maintaining the diameter of cerebral arterioles.

Pharmacological manipulations of type 1 nNOS neuron activity

As we saw expression of DREADDs primarily in type 2 nNOS neurons, we wondered how activation of type 1 nNOS neurons might affect arteriole dynamics. Type 1 nNOS neurons are unique among cortical neurons in that they express the receptor for Substance P (NK1R) (*Vruwink et al., 2001*; *Tomioka et al., 2005*; *Tomioka and Rockland, 2007*; *Gerashchenko et al., 2008*; *Kilduff et al., 2011*; *Kubota et al., 2011*; *Dittrich et al., 2012*; *Dittrich et al., 2015*; *Endo et al., 2016*; *Williams et al., 2019*; *Williams et al., 2018*), whose activation drives depolarization and spiking (*Dittrich et al., 2012*; *Endo et al., 2016*). As multiple single-cell genomics studies have shown there is no NK1R expressed in mouse cerebral vascular cells or in glial cells (*Vanlandewijck et al., 2018*; *Zeisel et al., 2018*), we can pharmacologically manipulate the activity of Type 1 nNOS neurons independently of other neurons by infusing SP, or an antagonist for the SP receptor, CP-99994 through a chronically implanted cannula. Infusions of CP-99994 caused non-significant changes in gamma-band power (*Figure 5A*, basal −5.4 ± 4.7%, p<0.28; locomotion, +7.3 ± 8.0%, p<0.37) and a non-significant decrease in basal arteriole diameter (−8.0 ± 7.2%, LME p<1, n = 7 mice, 28 vessels, *Figure 5B*) and locomotion-evoked dilation response (vehicle 13.7 ± 2.6%, CP-99994 9.7 ± 3.3%, LME p<1, n = 7 mice, 14 arterioles in FL/HL representation, *Figure 5C*). The lack of a substantial effect suggests that either basal activation of the Substance P receptors in the cortex is low, generating a floor effect and/or the basal activity of the type 1 nNOS neurons is low. When we activated the type 1 nNOS neurons via infusions of SP, we observed non-significant decreases in gamma-band power (*Figure 5D*, basal −20.0 ± 32.4%, p<0.53; locomotion, +5.2 ± 16.0%, p<0.73), but a substantial increase in basal diameter (+13.4 ± 4.4%, LME p<3.6×10^{-3}, n = 7 mice, 30 arterioles, *Figure 5E*), although the effect was not significant for locomotion-evoked responses (vehicle 13.0 ± 2.2%, SP 24.8 ± 4.7%, LME p<0.75, n = 7 mice, 14 arterioles in FL/HL representation, *Figure 5F*). To test the hypothesis that the Substance P facilitated dilation was mediated by increases in neural activity, we co-infused SP with muscimol to block local neural activity, and observed a reduction of the arteriole diameter (−20.0 ± 14.9%, LME p<3.4×10^{-7}, n = 5 mice, 27 arterioles, *Figure 5G*) and no locomotion-evoked dilation (vehicle 14.2 ± 3.0%, SP+muscimol −14.5 ± 3.7%, LME p<2.8×10^{-3}, n = 5 mice, seven arterioles in FL/HL representation, *Figure 5H*), consistent with the action of SP being mediated through local neural activity. These results suggest that type 1 nNOS neurons play an important role in NO-mediated changes in arteriole diameter.

Role of astrocytes and inwardly rectifying potassium channels

In addition to nitric oxide, there are multiple vasodilatory pathways that have been implicated in signaling the vasculature (*Attwell et al., 2010*; *Otsu et al., 2015*; *Bazargani and Attwell, 2016*; *Drew, 2019*). We first examined how chemogenetic modulation of astrocytes impacted basal and evoked arterial dilations (*Figure 5—figure supplement 1*). We found no significant modulation of arteriole diameter when either G(i)- or G(q)-coupled DREADDs on astrocytes were activated, consistent with previous reports that did not see coupling between astrocytes and evoked arterial responses (*Nizar et al., 2013*; *Bonder and McCarthy, 2014*; *Tran et al., 2018*). This does not rule out an astrocytic role for the control of the cerebral vasculature, as the signaling could work via mechanisms that are not coupled to G-protein signaling.

Recent reports have implicated inwardly-rectifying potassium channels in the capillary bed in mediating functional hyperemia (*Longden et al., 2017*). To test the role of these channels in basal and evoked arterial diameter control, we infused Ba^{2+} or ML-133 (*Longden and Nelson, 2015*), blockers of inwardly rectifying potassium channels. We found that both of these inwardly rectifying K$^+$ channel blockers drove very large increases in neural activity (Ba^{2+}, *Figure 5—figure supplement 2*: basal +88.3 ± 44.5%, p<0.01; locomotion, +145.6 ± 86.1%, p<0.02; and ML-133 S12E: basal +147.2 ± 77.7%, p<0.01; locomotion, +157.7 ± 86.4%, p<0.01). These observations of large increase
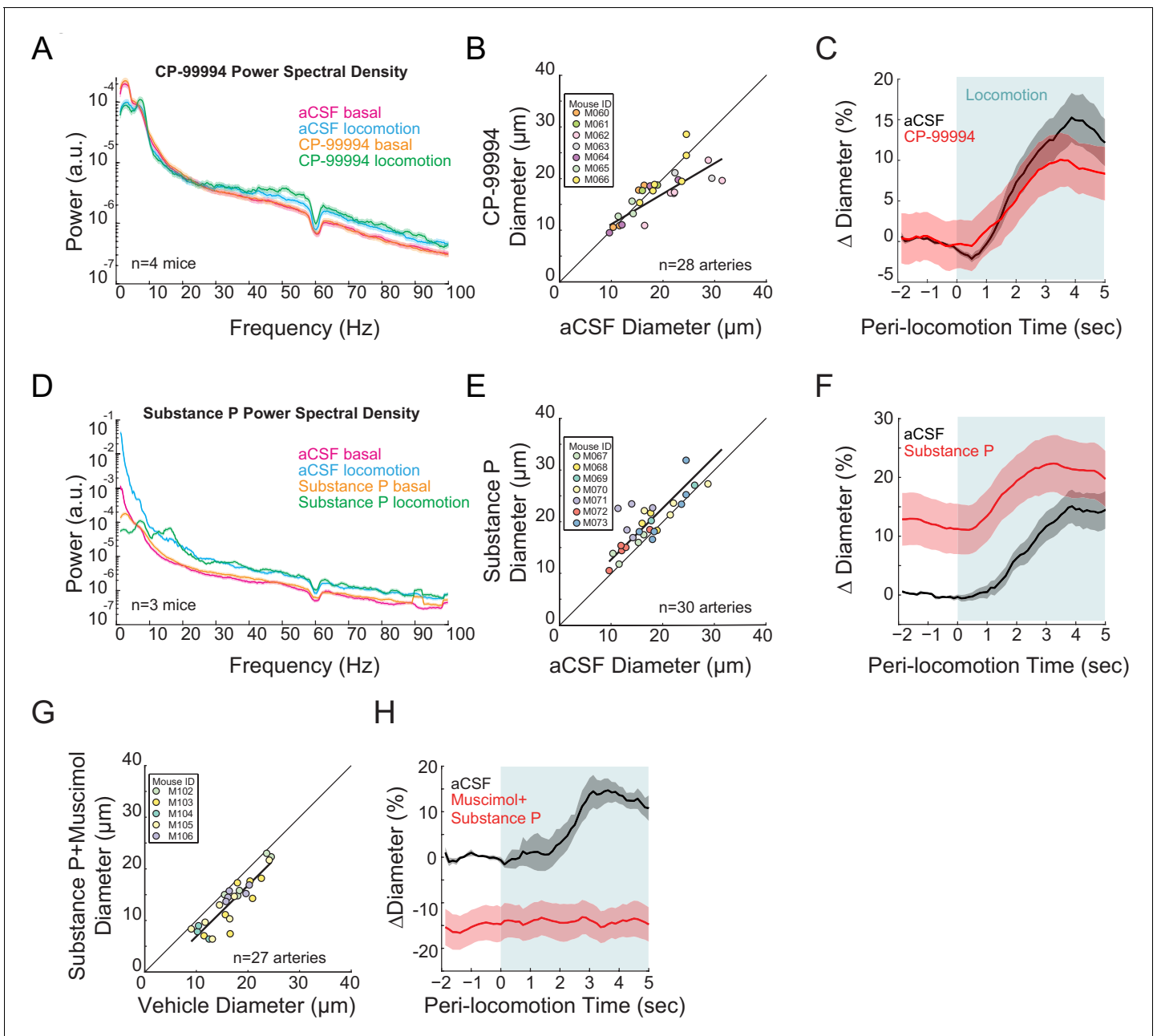
Figure 5. Type I nNOS expressing neurons control basal arteriole diameter. Data in **A-C** are from mice after local CP-99994 infusions, which will block the excitatory Substance P receptors on type1 nNOS neurons, data in **D-E** is from mice after Substance P infusions, which will excite Type1 nNOS neurons. (**A**) LFP power spectra during stationary (basal) and locomotion periods after CP-99994 infusion, normalized to vehicle infusion in the same mouse. (**B**) Plot of basal arteriole diameter after vehicle (x-axis) versus CP-99994 infusion (y-axis). (**C**) Population locomotion-triggered averages after vehicle or CP-99994 infusions for arterioles ≤ 25 µm in basal diameter. (**D**) LFP power spectra during stationary (basal) and locomotion periods after Substance P infusion, normalized to vehicle infusion in the same mouse. (**E**) Plot of basal arteriole diameter after vehicle infusion (x-axis) versus Substance P infusion (y-axis). (**F**) Population locomotion-triggered averages after vehicle or Substance P infusions for arterioles ≤ 25 µm in basal diameter. (**G**) Plot of basal arteriole diameter after vehicle infusion (x-axis) versus muscimol and Substance P infusion (y-axis). (**H**) Locomotion-triggered averages after vehicle or muscimol/Substance P infusions for arterioles ≤ 25 µm in basal diameter.

The online version of this article includes the following figure supplement(s) for figure 5:

Figure supplement 1. No significant effect of chemogenetic manipulation of astrocytes on basal vessel diameter or neural activity.

Figure supplement 2. Kir-channel blockers increase in neural activity and basal arterial diameter.

in basal and evoked neural activity are consistent with previous work that has shown that barium increases the activity of neurons in the awake cortex (*Harnett et al., 2013*). Barium is known to block inwardly rectifying potassium channels found on neurons, such as KIR2.1 (*Alagem et al., 2001*), Kir2.2 (*Amarillo et al., 2014*), and Kir2.3 (*Schram et al., 2003*). Blocking these channels will increase neural excitability, so it is not surprising that barium infusions increase overall neural activity. Blocking inwardly rectifying K$^+$ channels drove basal arteriole dilation (*Figure 5—figure supplement 2*: +12.4 ± 17.2%, LME p<2.0×10^{-3}, n = 5 mice, 24 arterioles; S12F: +11.8 ± 17.0% LME p<3.7×10^{-4}, n = 5 mice, 36 arterioles), and this basal dilation partially occluded the locomotion-induced response (*Figure 5—figure supplement 2*: vehicle 15.1 ± 2.7%, BaCl$_2$ +20.2 ± 5.3%, LME p<1, n = 5 mice, 16 arterioles in FL/HL representation and *Figure 5—figure supplement 2*: vehicle 14.01 ± 3.0%, ML-133 +21.5 ± 5.8%, LME p<1, n = 5 mice, 26 arterioles in FL/HL representation). As with chemogenetic increases in pan-neuronal activity (*Figure 2*), the increase in neural activity by barium drove a baseline dilation that nearly occluded the locomotion-induced response.

Because of the large increase in neural activity caused by blockade of inwardly rectifying potassium channels in the awake brain, and the likely release of vasodilator resulting from this increase in activity, it is hard to parse out any effects mediated by blockade of inward rectifying channels on the vasculature without transgenic models where the inwardly rectified channels are selectively removed from the vasculature (*Longden et al., 2017*). These results, along with the lack of effects of manipulation of G-protein-coupled pathways in astrocytes on arterial diameter highlight the need for the development of innovative manipulations of signaling pathways in astrocytes and endothelial cells as has been so successfully used for neurons.

Comparison of pial and penetrating arteriole basal and evoked diameter changes

It is informative to compare the responses of pial and penetrating arterioles to the manipulations performed here. We saw some differences between pial and penetrating arterioles, both in changes to their basal diameters, and in locomotion-evoked dilations. When we looked at basal diameter changes, we saw a significantly smaller constriction of penetrating arterioles than pial arterioles with muscimol infusions (*Figure 6A*). With pan-neuronal excitatory DREADDs, we saw a significantly smaller dilation in penetrating arterioles than in the pial arteries (*Figure 6D*). For all other manipulations, which in general produced smaller changes than muscimol and pan-neuronal excitatory DREADDs, there was no significant difference in the induced basal diameter changes between penetrating and pial arteries.

We then examined the percentage change in diameter during locomotion in pial and penetrating arterioles, here defined as the change from the respective pre-locomotion baseline normalized by the pre-locomotion baseline, for each of the manipulations. For this metric, a manipulation that causes a 10% constriction of baseline and shows a dilation of 5% above the control baseline will have a 15% locomotion-induced dilation (*Figure 6—figure supplement 1*). If the vessel has a 10% baseline dilation and during locomotion dilates to 15% above the control baseline, the percentage change will be 5%. This metric only captures the locomotion-induced dilation component and differs from the measures of dilation reported in the sections above, which included the effects of the baseline shift in diameter. When we looked at all the control condition (vehicle injections and aCSF infusions *Figure 6—figure supplement 2*), we saw a large and substantial difference in the pial arterial dilation versus the penetrating arteriole dilation (17.57 ± 9.35% pial vs. 6.79 ± 6.54% penetrating, LME p<8×10^{-37}). This difference is consistent with previous measurements of pial and penetrating arteriole dynamics during locomotion (*Gao et al., 2015*), so we treated penetrating and pial arteries as separate groups for further statistical analysis. We then compared the percentage diameter change during locomotion for pial arterioles and penetrating arterioles (*Figure 6—figure supplement 2*). With this metric, we saw significant differences in the locomotion-evoked responses of pial arterioles with muscimol, pan-neuronal excitation (hsyn-Gq), excitation of pyramidal neurons (CaMKIIa-Gq), inhibition of nNOS neurons (nNOS-Gi) and L-NAME. Interestingly, the expression of excitatory DREADDs in pyramidal neurons and pan-neuronally had the paradoxical effect of decreasing the amplitude of the locomotion-evoked dilation when quantified relative to its within treatment baseline. This result can be explained by the increased baseline neuronal activity increasing baseline arteriole diameters while not extending the maximum amplitude of arterial dilations. However, none
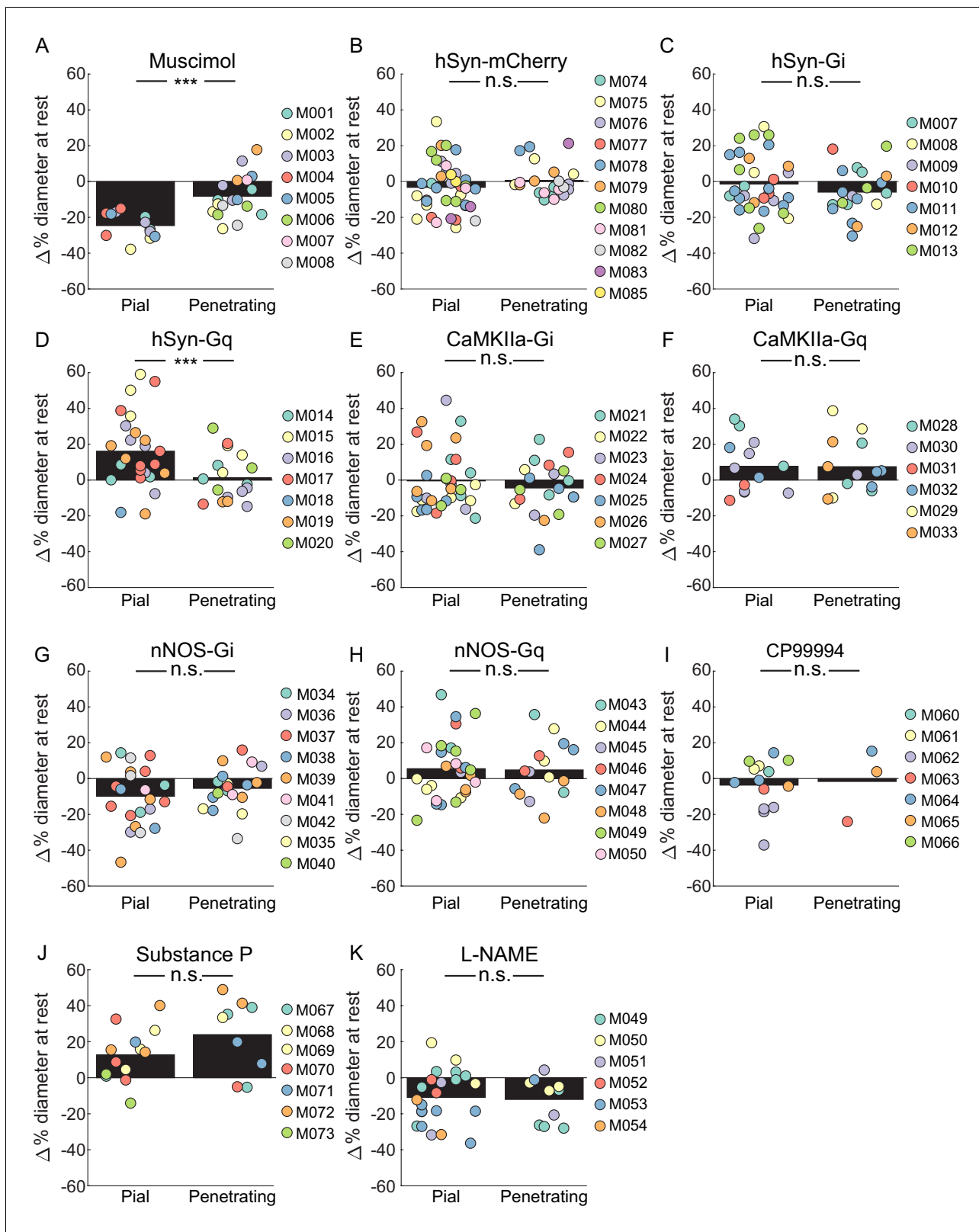
Figure 6. Comparisons of the effects of various manipulations on the basal diameters of pial and penetrating arterioles. (**A**) Comparison of change in resting vessel diameter in penetrating and pial arteries after Muscimol infusion. There was a significant difference in the change of baseline diameter between pial and penetrating arteries with pial arteries displaying a larger change. (LME p<1.5 × 10−6, n = 8 mice, 12 pial, 18 penetrating vessels). (**B**) Comparison of change in resting vessel diameter in penetrating and pial arteries in hSyn-mCherry-expressing animals after CNO infusion. No significant

Figure 6 continued on next page

Figure 6 continued

difference was observed in change in baseline diameter between pial and penetrating arteries (LME p<0.25, n = 11 mice, 40 pial, 22 penetrating vessels). (C) Comparison of change in resting vessel diameter in penetrating and pial arteries in hSyn-Gi expressing animals after CNO infusion. No significant difference was observed in change in baseline diameter between pial and penetrating arteries. (LME p<0.3, n = 7 mice, 33 pial, 20 penetrating vessels). (D) Comparison of change in resting vessel diameter in penetrating and pial arteries in hSyn-Gq expressing animals after CNO infusion. There was a significant difference between the change in baseline diameter between pial and penetrating arteries with pial arteries displaying a larger change (LME p<0.001, n = 7 mice, 25 pial, 17 penetrating vessels). (E) Comparison of change in resting vessel diameter in penetrating and pial arteries in CaMKIIa-Gi expressing animals after CNO infusion. No significant difference was observed in change in baseline diameter between pial and penetrating arteries. (LME p<0.5, n = 7 mice, 33 pial, 20 penetrating vessels). (F) Comparison of change in resting vessel diameter in penetrating and pial arteries in CaMKIIa-Gq expressing animals after CNO infusion. No significant difference was observed in change in baseline diameter between pial and penetrating arteries. (LME p<1, n = 6 mice, 13 pial, 13 penetrating vessels). (G) Comparison of change in resting vessel diameter in penetrating and pial arteries in nNOS-Gi expressing animals after CNO infusion. No significant difference was observed in change in baseline diameter between pial and penetrating arteries. (LME p<0.3, n = 9 mice, 22 pial, 19 penetrating vessels). (H) Comparison of change in resting vessel diameter in penetrating and pial arteries in nNOS-Gq expressing animals after CNO infusion. No significant difference was observed in change in baseline diameter between pial and penetrating arteries. (LME p<1, n = 8 mice, 28 pial, 15 penetrating vessels). (I) Comparison of change in resting vessel diameter in penetrating and pial arteries after CP99994 infusion. No significant difference was observed in change in baseline diameter between pial and penetrating arteries (LME p<1, n = 7 mice, 14 pial, three penetrating vessels). (J) Comparison of change in resting vessel diameter in penetrating and pial arteries after Substance P infusion. No significant difference was observed in change in baseline diameter between pial and penetrating arteries (LME p<0.15, n = 7 mice, 13 pial, 9 penetrating vessels). (K) Comparison of change in resting vessel diameter in penetrating and pial arteries after L-NAME infusion. No significant difference was observed in change in baseline diameter between pial and penetrating arteries (LME p<0.5, n = 6 mice, 22 pial, 10 penetrating vessels).

The online version of this article includes the following figure supplement(s) for figure 6:

Figure supplement 1. Schematic showing the calculation of the locomotion-evoked component of the diameter change.
Figure supplement 2. Locomotion triggered average diameter changes relative to locomotion diameter.

of our manipulations produced a significant change in the locomotion-evoked diameter change of penetrating arterioles from the control condition (*Figure 6—figure supplement 2*).

Overall, the locomotion-evoked changes in penetrating arteriole diameters were smaller than those in the pial arteries, and the size of the penetrating arteriole dilations were not affected by our manipulations. The difference observed between penetrating and pial arterioles cannot be due to imaging artifacts, as sub-micron cellular structures like spines and microglial processes can be imaged at this depth with a thinned skull window (*Drew et al., 2010b*; *Shih et al., 2012a*), and our diameter measurement algorithm (see Materials and methods) has been validated to work robustly in much lower signal-to-noise regimes than present here (*Gao and Drew, 2014*). There are several non-exclusive possibilities for the differences between the responses of pial and penetrating arteries to behavioral and experimenter-evoked changes in neural activity. One possible reason for this difference could be that penetrating arterioles are less sensitive to vasodilators, with a less steep voltage-diameter relationship that pial arterioles. As there are differences in mural cell morphology at different levels of the arteriole tree (*Hartmann et al., 2015*), it is possible that there are some previously unobserved differences in the smooth muscle or endothelial cells between penetrating and pial arteries. When mice are anesthetized with the powerful vasodilator isoflurane, pial and penetrating arteries dilate to the same extent, suggesting that the vessels have the same maximal dilation (*Gao et al., 2015*). The diameter of arterioles is linearly related to the membrane potential of smooth muscle cells (*Wölfle et al., 2011*), and any electrical signals at one point are conducted via gap junctions up to several hundred microns away (*Segal, 2005*; *Bagher and Segal, 2011*; *Hald et al., 2012*). As the pial arteries may be further up the arterial tree than penetrating arteries, they will be also integrating signals from many more smaller vessels (*Segal, 2000*; *Welsh et al., 2018*), and this may account for the differences in the amplitudes of the responses of the two vessel types. Another possibility could be the spatial location of the generation of the vasodilator(s) relative to the arterioles, particularly in the case of nitric oxide. Simulation of NO diffusion and degradation dynamics in the tissue have shown that NO production needs to be very close (of order microns to tens of microns) to the arteriole in order to exert an appreciable dilatory effect (*Haselden et al., 2020*). It could be that NO is produced closer to pial vessel (potentially in the processes of more superficial type two neurons), than near the penetrating arterioles in the superficial layers. Finally, the different mechanical environments of the pial and penetrating arterioles may account for their differing responses. The pial arterioles are surrounded by CSF (*Abbott et al., 2018*), whereas the

penetrating arterioles are surrounded by a thin paravascular space (*Iliff et al., 2012*) filled with collagen fibers tethering the artery to the brain (*Roggendorf and Cervós-Navarro, 1977*). When the smooth muscle cells surround pial arteries relax, the vessel's dilation need only displace CSF, which has viscosity near that of water, while dilation (or constriction) of penetrating arterioles must displace (or pull upon) the viscoelastic brain tissue (*Goriely et al., 2015*; *Weickenmeier et al., 2018a*; *Weickenmeier et al., 2018b*; *Kedarasetti et al., 2020*). The viscoelasticity of brain tissue will function as an ultra-low-pass mechanical filter on diameter changes of penetrating arterioles, reducing the amplitude of 'rapid' dilations (on the order of seconds), although allowing slower dynamics (on the order of minutes), which could explain why we saw similar changes in both pial and penetrating arterioles baseline (which take place over minutes), but no effects on the 'rapid' locomotion-evoked dilations. Studies in peripheral vascular structures have shown that when blood vessels are imbedded in tissue, the mechanics of the surround tissues dominates and reduces their dilation (*Fung et al., 1966*; *Liu et al., 2007*). Brain tissue is stiffer when the skull is intact than after a craniotomy (*Hatashita and Hoff, 1987*). Brain tissue exhibits strain-stiffening (becoming stiffer under pressure) (*Marmarou et al., 1975*; *Marmarou et al., 1978*), and locomotion is accompanied by an elevation of intracranial pressure (*Gao and Drew, 2016*; *Norwood et al., 2019*; *Eftekhari et al., 2020*). All these factors may exacerbate mechanical restriction of dilation by stiffening the brain tissue, preventing full expression of the arterial dilation to locomotion in penetrating arterioles. These results show that pial and penetrating arterioles display similar basal diameter changes for manipulations that produced moderate changes in diameter, although the locomotion-evoked changes in diameter of penetrating arterioles were not affected by any of the manipulations of neural activity. Elucidating the vascular, neural, and/or mechanical origins of the differences in the responses of pial and penetrating arterioles will be informative for understanding their roles in regulating cerebral blood flow (*Lorthois et al., 2011*; *Gould et al., 2017*; *Schmid et al., 2017*).

Locomotion drives robust Ca^{2+} responses in nNOS neurons

If nNOS neurons contribute to the locomotion-induced dilation of arteries, then we would expect their activity to increase during locomotion. Electrophysiological recordings have shown that voluntary locomotion drives large increases in the activity of pyramidal neurons and interneurons in FL/HL representation (*Figure 1—figure supplement 1*; *Zhang et al., 2019*), but it is not known if nNOS-positive interneurons exhibit increased activity, as their activity cannot be separated out electrophysiologically. To determine how nNOS-positive interneuron activity is affected by locomotion, we used fiber photometry (*Schulz et al., 2012*) to simultaneously monitor the activity of nNOS neurons expressing GCaMP6s (*Chen et al., 2013*) and local cerebral blood volume deep in the parenchyma, which was labeled with an intravenous injection of TRITC dextran (*Cerri et al., 2019*). Calcium signals have been shown to be strong quantitative predictors of hemodynamic signals (*Aydin et al., 2020*). Fiber photometry will record bulk calcium signals from the processes and cell bodies of a specific neuronal cell type, and these calcium signals should correlate with nitric oxide production (whose synthesis is known to be calcium dependent) in nNOS-expressing neurons. Fiber photometry is not imaging forming, and will report the summed fluorescence of neurons within ~200 µm from the tip of the fiber (*Pisanello et al., 2019*), so the contributions of type 1 and type 2 nNOS neurons cannot be differentiated. However, given the low density of type 1 nNOS neurons, the signal is likely to be primarily from type 2 nNOS neurons. We corrected for the absorbance of fluorescence by hemoglobin (*Gunaydin et al., 2014*; *Cerri et al., 2019*) in the blood using the TRITC signal, and validated this method on mice that expressed GFP ubiquitously (*Okabe et al., 1997*; *Figure 7—figure supplement 1*). The slow (on the timescale of tens to hundreds of seconds) rise and fall of the CBV signals is due to the venous component. The venous contribution to the CBV signal is known to be larger than the arterial component (*Kim et al., 2007*; *Huo et al., 2015b*; *Huo et al., 2015a*) and have slower dynamics than the arterial component (*Kim et al., 2007*; *Drew et al., 2011*; *Moon et al., 2013*; *Gao et al., 2015*; *Huo et al., 2015b*; *Huo et al., 2015a*; *Gao and Drew, 2016*), particularly in the parenchyma (*Kim and Kim, 2010*). We found that calcium signals from GCaMP expressed pan-neuronally, in pyramidal neurons, and in nNOS-positive neurons greatly increased during locomotion (*Figure 7A–C,E* Population GCaMP intensity change in z-units: hSyn: 2.51 ± 0.15, LME difference from CaMKII: p<0.44; CaMKII: 2.59 ± 0.38; nNOS: 1.94 ± 0.37, LME difference from CaMKII: p<1e-3). Activity in all these neuron types was correlated with vasodilation (*Figure 7—figure supplement 2*, CaMKII: 0.60 ± 0.17; hSyn: 0.54 ± 0.14, LME difference from CaMKII: p<0.7;
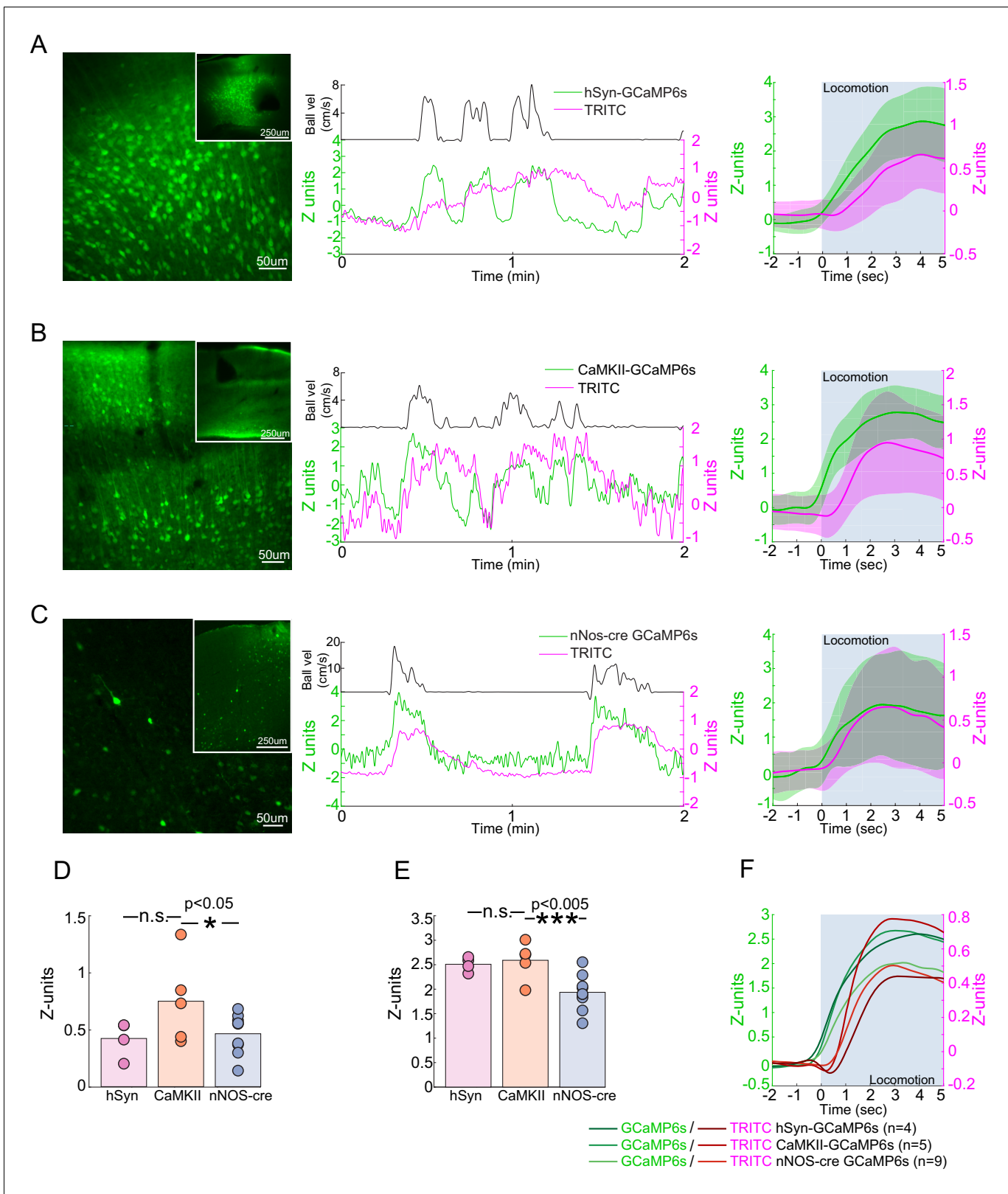
Figure 7. Locomotion-evoked Ca^{2+} signals in neurons. (A–C) Left, a representative image of cortex taken of AAV-hSyn-GCaMP6s in C57BL/6J mice (A), AAV-CaMKII-GCaMP6s in C57BL/6J mice (B) and AAV-Syn-FLEX-GCaMP6s in nNOS-cre mice. Note that there are substantially fewer cells labeled in AAV-Syn-FLEX-GCaMP6s in nNOS-cre mice. Center, a representative trace of TRITC (blood volume - magenta) and GCaMP6s (green) changes evoked by a single locomotion event (black trace above). Right, average locomotion-evoked blood volume and GCaMP6s changes of events >5 s and <10 s in

Figure 7 continued on next page

Figure 7 continued

duration from the example animal. Locomotion period shaded in blue. (D) Population average locomotion-evoked blood volume change. Bars are population mean of each GCaMP6s sub-type; circles are individual animal averages. (E) Population average locomotion-evoked GCaMP6s fluorescence change. Bars are population mean of each GCaMP6s sub-type; circles are individual animal averages. (F) Population average trace of locomotion-evoked changes in blood volume (red) and GCaMP (green) fluorescence. Period of locomotion is shaded in blue.

The online version of this article includes the following figure supplement(s) for figure 7:

Figure supplement 1. Locomotion-evoked Ca^{2+} signals in nNOS neurons, correction of photobleaching and hemodynamic attenuation of GCaMP signals.

Figure supplement 2. Cross-correlation, coherence, and signal-to-noise comparisons for fiber photometry signals.

Figure supplement 3. Sustained locomotion-evoked Ca^{2+} signals in nNOS neurons during long duration locomotion events.

nNOS: 0.43 ± 0.11, LME difference from CaMKII: $p<0.02$). We also asked if the activity of nNOS neurons were sustained during locomotion, as there is a sustained dilation of arteries during locomotion (*Huo et al., 2015b*; *Gao and Drew, 2016*), and it has been suggested that the response of nNOS neurons is transient (*Iadecola, 2017*). We found that the responses of nNOS neurons were sustained throughout the locomotion bouts (*Figure 7—figure supplement 3* nNOS population GCaMP intensity change in z-units, 10 s: 1.90 ± 0.46, LME: $p<0.01$, 15 s: 1.84 ± 0.52, LME: $p<0.97$, 30 s: 1.56 ± 0.40, LME: $p<0.72$).

When we compared the change in the TRITC fluorescence (a measure of blood volume change) evoked by locomotion in GCaMP-nNOS mice to those in mice expressing GCaMP in pyramidal neurons we found a significantly smaller responses than in mice with calcium indicators in pyramidal neurons (*Figure 7D* Population TRITC intensity change (z-units), hSyn: 0.42 ± 0.16, LME difference from CaMKII: $p<0.08$, CaMKII: 0.75 ± 0.38, nNOS: 0.46 ± 0.18, LME difference from CaMKII: $p<0.04$). Pan-neuronal expression of GCaMP also decreased the CBV change, though not significantly. We do not know the origin of the difference between hemodynamic responses of nNOS and CaMKII-GCaMP mice, but one plausible cause could be that smaller locomotion-evoked response might be caused by the expression of a calcium indicator in the nNOS neurons. Calcium indicators will buffer calcium levels (*Higley and Sabatini, 2008*; *McMahon and Jackson, 2018*), reducing the amplitude of activity-dependent calcium transients by competing with endogenous calcium-binding proteins. This calcium buffering could reduce the production of NO in cells expressing the indicator because the activity of nNOS is calcium-dependent (*Garthwaite, 2008*).

There are several caveats to these experiments. The fluorescence signals from nNOS neurons, whether measured as absolute fluorescence or in the absolute changes in fluorescence, was substantially smaller than the signals from pan-neuronally expressed GCaMP or GCaMP expressed pyramidal neuron localized GCaMP signals. This is a consequence of the much lower number of GCaMP-nNOS neurons than the with the pan-neuronal or pyramidal neuron specific promoters (*Figure 7A–C*). This large difference in the absolute signals for these different conditions means that it would be inappropriate to draw any strong conclusions in differences in the calcium signal amplitudes or in correlation coefficients between blood volumes and neural activity. Calcium indicators are qualitative indicators of neural activity, as simultaneous calcium imaging and electrophysiology has found that the correlation between calcium signals and spiking activity is moderate (*Harris et al., 2016*; *Theis et al., 2016*; *Pachitariu et al., 2018*), and there are likely cell-type specific differences in calcium levels, indicator expression, and coupling of calcium changes to spiking that makes it untenable to make quantitative comparisons across calcium measurements of activity across different cell types. Different neuronal subtypes are known to have differing calcium buffering (*Lee et al., 2000*; *Egger and Stroh, 2009*; *Matthews et al., 2013*) and nitric oxide synthase expressing neurons show low levels of endogenous calcium binding proteins (*Dun et al., 1994*). These results show that nNOS neurons, like pyramidal neurons and other interneurons (*Zhang et al., 2019*), increase their activity during locomotion.

Relationship between neural activity and arterial dilation

One of the key utilities of hemodynamic imaging is that it allows us to make inferences about neural activity. As we have measured both neural activity and arterial diameter for multiple different perturbations, we sought to understand the relationship between them for different manipulations in pial arteries (*Figure 8—figure supplement 1*). We plotted the arterial diameter and gamma band power

changes for each of the manipulations from the vehicle basal condition in *Figure 8*, with the basal and locomotion conditions connected by a line. A horizontal (left-right) shift means that neural activity is changed without a corresponding change in arterial diameter, while any vertical shift of the points means that there is change in arterial diameter without a corresponding change in neural activity. If there was a perfect, one-to-one ratio between gamma band power and arterial diameter, all of these points would lie along a line or a curve. If this is the case, by knowing the change in arterial diameter, one could infer the change in neural activity accurately from knowing the changes in arterial diameter. At the other extreme, if there were no relationship between neural activity and diameter, the points would be a shapeless blob. In this situation, it is not possible to infer neural activity from a change in arterial dilation.

Within all the manipulations, we found that the increase in neural activity accompanying locomotion was accompanied by an arterial dilation. However, across conditions there was only a weak relationship between neural activity and arterial diameter. For example, the gamma band power was
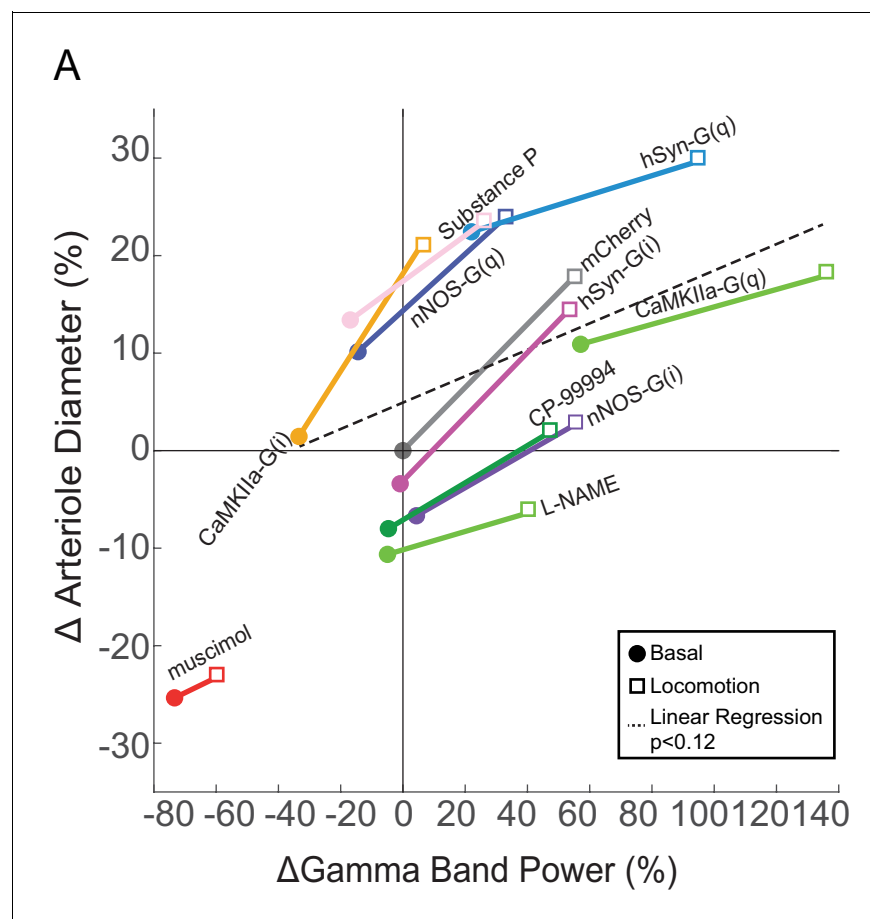
Figure 8. Relationship between neural activity and arterial diameter. (**A**) Summary showing the gamma-band power vs. arteriole diameter, normalized to the relevant vehicle control for each condition. Lines connect mean basal and locomotion neural/arterial responses for each condition. Note the large differences in arterial diameter for similar levels of neural activity (e.g. nNOS-G(q) vs. nNOS-G(i)). A linear regression of all the points in the physiologically-relevant range (excluding muscimol), was not significant (p<0.12). For chemogenetic manipulations, neural activity and basal arterial dilation have been shifted so that the reporter virus expressing animals (mCherry) are centered at the origin.

The online version of this article includes the following figure supplement(s) for figure 8:

Figure supplement 1. Examples of chemogenetic and pharmacological effects on arteriole diameters.
Figure supplement 2. Relationship between arterial diameter and LFP power at lower frequencies.
Figure supplement 3. The effects of chemogenetic and pharmacological infusions on evoked arterial diameter changes normalized to the baseline within condition.

similar for both CaMKII-G(i) mice during locomotion and stationary nNOS-G(i) mice, but there were very large (~30%) differences in the arterial diameter. As another example, the change in arterial diameter was the same for stationary CaMKII-G(i) mice as for nNOS-G(i) during locomotion, even though there was an approximately threefold difference in neural activity A linear regression between change in neural activity and change in diameter (excluding the outlier muscimol) reveals no significant relationship between the two (p<0.12). We also looked at the relationship between power in other bands in the LFP (1–10 Hz and 10–40 Hz) and there was either a very weak relationship (for 10–40 Hz, p<0.04, R^2 = 0.04) or no significant relationship (1–10 Hz, p<0.05) (*Figure 8—figure supplement 2*). The lack of a strong relationship between arteriole diameter and LFP, which reports the summed activity of all neurons, though with large pyramidal neurons giving a disproportionally large contribution (*Lindén et al., 2011*; *Einevoll et al., 2013*; *Pesaran et al., 2018*), implies that a small set of nNOS expressing neurons can influence arterial diameter without influencing the LFP and vice versa.

Discussion

Here, we showed that neural activity controls not only evoked arterial dilations, but also basal arterial diameter. Increases or decreases in overall neural excitability drove corresponding basal dilations or constrictions of arterioles. Surprisingly, modulation of the activity of pyramidal neurons had only small effects on basal and evoked arterial dilations. Neurons that express nNOS played an important role in controlling the basal dilation, as chemogenetic inhibition of nNOS positive neurons or NOS inhibition produced a change in basal diameter that was about half as big as seen when silencing activity with muscimol. Although nNOS positive neurons play an important role in controlling arterial diameter, changing their activity makes little contribution to the LFP. These results extend previous work showing that optogenetic stimulation of all interneurons (*Anenberg et al., 2015*; *Uhlirova et al., 2016b*), and nNOS positive interneurons in particular (*Krawchuk et al., 2020*; *Lee et al., 2020*) drive robust vasodilation, with optogenetic stimulation of pyramidal neurons being able to drive only small vasodilations (*Vazquez et al., 2018*). The small effect of manipulations on pyramidal cell activity on basal arterial diameter suggests that nNOS-positive neurons either do not receive strong local pyramidal neuron input, as large changes in pyramidal neuron firing had only small effects on basal and evoked dilations, or these inputs undergo short-term synaptic depression (*Abbott et al., 1997*). When synaptic depression is present at a synapse, it will eliminate the effects of changes in background firing rate (such as those caused by DREADDs) and only transmit the percentage changes in rate. Under normal circumstances in the somatosensory cortex of the awake behaving mouse, the activity of these nNOS-positive neurons is likely correlated to the activity of nearby neurons, as with other neurons, nNOS neurons receive cholinergic modulatory inputs (*Williams et al., 2019*; *Williams et al., 2018*), and cholinergic input increases during locomotion (*Harrison et al., 2016*). Because the activity of nNOS-expressing neurons will be correlated with other neurons, this explains the observed correlations between neural activity and vasodilation. Though increases in blood flow are usually correlated with neural activity, this is not always the case. Hemodynamic signals can occur without corresponding detectable increases in neural activity (*Sirotin and Das, 2009*; *Cardoso et al., 2012*; *Cardoso et al., 2019*), and neural activity increases are not always followed by corresponding increases in blood flow (*Huo et al., 2014*; *Zhang et al., 2019*). In the striatum, increases in neural activity can be accompanied by vasoconstriction and decreases in blood flow (*Shih et al., 2009b*; *Shih et al., 2011*). There are other known mismatches between neural and hemodynamic signals in the visual cortex (*Maier et al., 2008*; *Boynton, 2011*). Our data suggest a mechanism underlying these cases of neurovascular decoupling. It is possible that these mismatches are found when the activity of the vasodilatory nNOS neurons diverges greatly from the rest of the neural population.

These results also show that it is critical to perform quantitative, within-vessel measurements or other calibrations when testing the role of specific signaling pathways on evoked vasodilation. Here, we were able to get absolute measures of arterial diameters for the same vessels under both control and the manipulation conditions. However, hemodynamic signals are often measured ratiometrically relative to the baseline in the given condition, and changes in baseline vessel diameter can confound these ratiometric signals (*Cohen et al., 2002*; *Figure 8—figure supplement 3*). Whenever responses in two different groups of subjects are compared (e.g. transgenic vs. wildtype), the potential for

changes in the baseline are a confound. However, any changes in the baseline in population can be detected by dilating the vessels with isoflurane (*Cudmore et al., 2017*) or CO_2 (*Hutchinson et al., 2006*), or testing the basal tone of the vessel in vitro (*Adebiyi et al., 2007*). These tests will reveal if the baseline changes, as the apparent maximal dilation/relaxation will be reduced. Our results show the critical importance of these controls when trying to establish the mechanisms and cellular underpinnings of neurovascular coupling.

There are several caveats to our work. First, the net effect of our chemogenetic manipulations on neural activity depend on the cellular machinery and network interactions in the local neural circuits. Because chemogenetic manipulations alter excitability via endogenous G-protein-coupled ion channels, there will be some variability in their effects between cell-types, and between G(i) and G(q) DREADDs in the same cells, as the amplitude of the excitability modulation depends on the compliment of ion channels present. Our viruses did not infect all nNOS neurons, and were not completely specific. Expression of chemogenetic proteins may also affect basal activity levels in neurons (*Saloman et al., 2016*), which is why whenever possible we have tried to use both pharmacological and chemogenetic manipulations (e.g. G(i)-DREADDs in nNOS neurons and NOS inhibitors) to generate converging lines of evidence. Additionally, increasing and decreasing the activity of a single neuron type does not always have symmetric effects on network activity due to interactions within the cortical circuit (*Phillips and Hasenstaub, 2016*). Similarly, pharmacological effects may not be symmetrical due to levels of baseline activity or modulatory tone. For example, Substance P receptors may have a low level of basal activation in the cortex of awake mice, so blocking them may only have a small effect on the activity of type 1 nNOS neurons in the cortex. In vitro studies have shown that activation of Substance P receptors drives large increases in activity (*Endo et al., 2016*; *Williams et al., 2019*; *Williams et al., 2018*), potentially accounting for the asymmetry of vascular responses to the application of blockers and activators of these receptors. Simulations have shown that the location of NO production relative to the arteriole has a large impact on its efficacy (*Haselden et al., 2020*), so the location of the infected neurons relative to the arterioles may cause some variability. We performed our experiments in awake mice, as anesthetics cause large decreases in brain metabolism, cardiovascular output, and ongoing neural activity (*Gao et al., 2017*), but there could be some variability associated with the mice being awake. However, the locomotion-evoked hemodynamic responses were not due to systemic changes in cardiovascular output, as the locomotion-evoked vasodilation is spatially localized to the FL/HL representation of the somatosensory cortex (*Huo et al., 2014*; *Huo et al., 2015b*; *Huo et al., 2015a*; *Zhang et al., 2019*), not affected by drugs that alter heart rate and blood pressure (*Huo et al., 2015a*), and blocked by local neural silencing (*Figure 1E*). Although we did not monitor heart rates here, head-fixed mice show heart rates comparable to freely moving mice (*Gehrmann et al., 2000*), and fluctuations in heart rates in head-fixed mice do not explain spontaneous and evoked changes in blood flow or vasodilation (*Drew et al., 2011*; *Winder et al., 2017*). None of the manipulations of neural activity used here produced significant changes in the amount of locomotion, so their effects cannot be attributed to changes in behavior. Because many of the manipulations of neural activity (i.e. CaMKIIa-G(i) DREADDs) resulted in minimal changes of arterial diameter across conditions, systemic fluctuations were unlikely to play a substantial role in our preparation. Interestingly, none of our manipulations substantially increased the sensory-evoked dilations above those in control conditions, although some drove large increases in neural activity and/or basal arterial diameter. It seems the dilations that occur during locomotion (~20% above the basal diameter) are near saturation for cerebral arteries under normal circumstances, as increasing the activity of all neurons or nNOS positive neurons were unable to raise the evoked dilation substantially above this level.

Our results suggest a model where approximately half of the dynamic range in the basal and evoked blood arterial diameter is controlled by a small group of neurons and the rest is controlled by other neurons and astrocytes. Any damage to or dysfunction of nNOS neurons could result in decreased basal blood flow, regardless of the metabolic need. Importantly, changes in activity patterns of these neurons will alter basal diameter of arteries, which is known to affect the amplitude of fMRI signals (*Cohen et al., 2002*). Simulations have shown that cerebral arteries account for approximately half of the resistance in the cerebral vasculature (*Schmid et al., 2017*; *Rungta et al., 2018*), so arterial diameter will play an important role in setting basal and evoked blood flow levels. There is a decline in the number of interneurons, particularly nNOS-expressing interneurons, with aging (*Miettinen et al., 1993*; *Necchi et al., 2002*), and the removal of their tonic vasodilatory signal could

contribute to decreases in cerebral blood flow that are thought to lead to dementia (*Wolters et al., 2017*). Indeed, alterations of nNOS expression have been implicated in Alzheimer's disease (*Han et al., 2019b*) and chronic stress (*Han et al., 2019a*). Protecting these neurons from insults and damage could be a promising strategy for preventing neurovascular disorders.

Materials and methods

Key resources table

Reagent type (species) or resource	Designation	Source or reference	Identifiers	Additional information
Strain, strain background (*Mus musculus*)	C57BL/6J	Jackson Labs	#000664	
Strain, strain background (*Mus musculus*)	B6.129-*Nos1*$^{tm1(cre)Mgmj}$/J	Jackson Labs	#017526	
Strain, strain background (*Mus musculus*)	FVB-Tg(*Aldh1l1*-cre/ERT2)1Khakh/J	Jackson Labs	#023748	
Strain, strain background (*Mus musculus*)	C57BL/6-Tg(CAG-EGFP)131Osb/LeySopJ	Jackson Labs	#006567	
Genetic reagent (Adeno-associated virus)	AAV5-CMV-Turbo RFP-WPRE-rBG	UNC vector core		
Genetic reagent (Adeno-associated virus)	AAV8-hSYN-HA-hM3D (Gq)-mCherry	Addgene	#50474-AAV8	
Genetic reagent (Adeno-associated virus)	AAV5-hSYN-HA-hM4D (Gi)- mCherry	UNC Vector Core		
Genetic reagent (Adeno-associated virus)	AAV5-CaMKIIa-hM3D (Gq)- mCherry	Addgene	#50476-AAV5	
Genetic reagent (Adeno-associated virus)	AAV5-CaMKIIa-hM4D (Gi)- mCherry	UNC Vector Core		
Genetic reagent (Adeno-associated virus)	AAV8-DIO-hM3D (Gq)-mCherry	Addgene	#44361-AAV8	
Genetic reagent (Adeno-associated virus)	AAV8-DIO-hM4D (Gi)-mCherry	Addgene	#44362-AAV8	
Genetic reagent (Adeno-associated virus)	AAV9-CaMKII-GCaMP6s	Addgene	#107790-AAV9	
Genetic reagent (Adeno-associated virus)	AAV8-syn-GCaMP-WPRE	Vigene	AAV8-syn-GCaMP-WPRE	
Genetic reagent (Adeno-associated virus)	AAV9-CaMKII-GCaMP6s	Addgene	#107790-AAV9 Viagene	
Antibody	Mouse monoclonal GAD-65 Antibody (A-3)	Santa Cruz Biotechnology	sc-377145	(1:200)
Antibody	Mouse monoclonal CaMKII Antibody (G-1)	Santa Cruz Biotechnology	sc-5306	(1:200)
Antibody	Rabbit polyclonal to GFAP	Abcam	ab7260	(1:200)
Antibody	Alexa Fluor 488 Goat Anti-Mouse IgG H and L	Abcam	ab150113	(1:500)
Antibody	Goat Anti-Rabbit IgG H and L	Abcam	ab6702	(1:500)
Antibody	Goat polyclonal nNOS	Abcam	ab1376	(1:200)
Chemical compound, drug	muscimol	Sigma-Aldrich	M1523	10 mM
Chemical compound, drug	L-NAME	Sigma-Aldrich	N5751	1 mM
Chemical compound, drug	Substance P	Tocris	1156	1 mM
Chemical compound, drug	CP-99994	Tocris	3417	8 mM
Chemical compound, drug	ML-133	Sigma-Aldrich	SML0190	10 µM
Chemical compound, drug	DMSO	Sigma-Aldrich	D8418	1%

Continued on next page

Continued

Reagent type (species) or resource	Designation	Source or reference	Identifiers	Additional information
Chemical compound, drug	$BaCl_2$	EMD Millipore	B1493816	100 µM
Chemical compound, drug	CNO	Sigma-Aldrich	C0832	2.5 mg/kg
Chemical compound, drug	FITC-dextran 70 kDa	Sigma-Aldrich	46945	50 µL at 5%
Chemical compound, drug	TRITC dextran 70kD	Sigma-Aldrich	T1162	50 µL at 5%
Software, algorithm	Pial vessel dimeter measurements	https://github.com/DrewLab/Surface-Vessel-FWHM-Diameter		
Software, algorithm	Penetrating vessel dimeter measurements	https://github.com/DrewLab/Thresholding_in_Radon_Space		
Software, algorithm	Red blood cell velocity measurements	https://github.com/DrewLab/MCS_Linescan		
Software, algorithm	2 P microscope control software	MCS, Sutter Instruments, Novato CA		
Software, algorithm	MATLAB	Mathworks, Natick MA		
Software, algorithm	Doric Neuroscience Studio	Doric Lenses, Quebec, Quebec Canada		

Animal procedures

This study was performed in strict accordance with the recommendations in the Guide for the Care and Use of Laboratory Animals of the National Institutes of Health. All procedures were performed in accordance with protocols approved by the Institutional Animal Care and Use Committee (IACUC) of Pennsylvania State University (protocol # 201042827). All surgeries were performed under isoflurane anesthesia and every effort was made to minimize suffering. Data were acquired from 209 mice (107 mice for 2PLSM imaging, 61 mice for electrophysiology, 21 mice for fiber photometry, and 20 mice for immunohistochemistry - see *Tables 1* and *2*) C57BL/6J mice, cre-nNOS mice (B6.129-*Nos1*$^{tm1(cre)Mgmj}$/J), C57BL/6-Tg(CAG-EGFP), and *Aldh1L1*-cre-mice (B6;FVB-Tg(*Aldh1l1*-cre/ERT2) 1Khakh/J Jackson Laboratory) between 3 and 8 months of age were used. Some mice received infusions of multiple drugs. Mice were given food and water ad libitum and maintained on 12 hr light/dark cycles in isolated cages during the period of experiments. All in vivo experiments were performed between 8:00 and 12:00 ZT. Sample size was chosen to be consistent with previous studies in the literature (*Zhang et al., 2019*; *Aydin et al., 2020*).

Virus injections

All viruses were obtained from UNC Vector Core, Addgene, or Vigene (see *Table 1*). For viral injections, mice were anaesthetized with isoflurane (5% induction, 2% maintenance) and placed in a stereotaxic rig. A small craniotomy was made over the FL/HL representation of the somatosensory cortex (0.75 mm caudal, 2.5 mm lateral from bregma). Using a pulled glass micropipette (30–50 µm tip diameter) and infusion pump (Harvard Apparatus, Holliston, MA), we microinjected 500 nanoliters (at a rate 100 nl/min) of the adeno-associated viral (AAV) vectors (see *Table 1*) ~300 µm beneath the cortical surface. After the viral injections were completed, the glass micropipette was kept in place for 10 min before withdrawal. The skin was sutured, and mice were returned to their home cage. Four weeks after AAV injections, we performed surgeries for electrode or window implantation, or perfusion for immunohistochemistry.

Window, electrode, and cannula implantation procedures

Mice were anesthetized with isoflurane and the scalp was resected. A custom-made titanium metal bar (https://github.com/DrewLab/Mouse-Head-Fixation) was fixed to the skull with cyanoacrylate glue (Vibra-Tite, 32402) and dental cement just posterior to the lambda cranial suture. A 4–8 mm^2 area polished and reinforced thinned-skull window was created over the forepaw/hindpaw representation of somatosensory cortex on the right hemisphere, as described previously (*Drew et al., 2010b*; *Gao and Drew, 2016*; *Winder et al., 2017*). The thinned area was polished with size 3F grit (Covington Engineering, Step Three 3 F-400) and reinforced with a fitted #0 glass coverslip

Table 1. AAV-injected mice.

AAV-injected mice	# mice (vessels) for 2-photon imaging	# mice for chronic electrophysiology	Immunohistochemistry	Fiber photometry
C57BL/6J: AAV5-CMV-TurboRFP-WPRE-rBG (UNC Vector Core)	12 mice (56 vessels)	Four mice	Three mice	
C57BL/6J: AAV8-hSYN-HA-hM3D(Gq)-mCherry (Addgene #50474-AAV8)	Seven mice (37 vessels)	Three mice	Three mice	
C57BL/6J: AAV5-hSYN-HA-hM4D(Gi)- mCherry (UNC Vector Core)	Seven mice (45 vessels)	Three mice	Two mice	
C57BL/6J: AAV5-CaMKIIa-hM3D(Gq)- mCherry (Addgene # 50476-AAV5)	Six mice (41 vessels)	Four mice	Two mice	
C57BL/6J: AAV5-CaMKIIa-hM4D(Gi)- mCherry (UNC Vector Core)	Seven mice (38 vessels)	Five mice	Two mice	
B6.129-Nos1$^{tm1(cre)Mgmj}$/J: AAV8-DIO-hM3D(Gq)-mCherry in nNOS-cre mice (Addgene #44361-AAV8)	Eight mice (52 vessels)	Four mice	Two mice	
B6.129-Nos1$^{tm1(cre)Mgmj}$/J: AAV8-DIO-hM4D(Gi)-mCherry in nNOS-cre mice (Addgene #44362-AAV8)	Nine mice (49 vessels)	Five mice	Two mice	
B6;FVB-Tg(Aldh1l1-cre/ERT2)1Khakh/J: AAV8-DIO-hM4D(Gi)-mCherry in astrocyte-cre mice (Addgene #44362-AAV8)	Five mice (24 vessels)	Three mice	Two mice	
B6;FVB-Tg(Aldh1l1-cre/ERT2)1Khakh/J: AAV8-DIO-hM4D(Gi)-mCherry in astrocyte -cre mice (Addgene #44362-AAV8)	Seven mice (31 vessels)	Four mice	Two mice	
C57BL/6J: AAV9-CaMKII-GCaMP6s (Addgene)				Five mice
C57BL/6J: AAV8-syn-GCaMP-WPRE (Vigene)				Four mice
B6.129-Nos1$^{tm1(cre)Mgmj}$/J: AAV9-CaMKII-GCaMP6s (Addgene)				Nine mice
C57BL/6-Tg(CAG-EGFP)131Osb/LeySopJ (Jackson Labs)				Three mice

(Electrode Microscopy Sciences, #72198). Self-tapping screws (#000, 3/32', JI-Morris, Southbridge, MA) were placed into the contralateral parietal and ipsilateral frontal bone to stabilize the skull. The titanium bar and screws were secured with black dental acrylic resin. The animals were allowed 2–3 days to recover before habituation.

For electrode or cannula implantation, small (<0.5 mm diameter) craniotomies were made to insert the stereotrode or cannula (Plastics One, C315DCS, C315GS-4) into the upper layers of cortex near the FL/HL representation of cortex. The cannula was attached to the skull and headbar with cyanoacrylate glue and dental acrylic. Implanted cannulas do not alter the hemodynamic response (*Winder et al., 2017*). The position of the cannula within the window was located relative to the large surface vessels, which are clearly visible on wide-field images taken under a surgical

Table 2. Infused mice.

Infused mice	# mice (vessels) for two-photon imaging	# mice for chronic Electrophysiology
C57BL/6J: Muscimol (10 mM)	Nine mice (26 vessels)	Three mice
C57BL/6J: L-NAME (1 mM)	Six mice (36 vessels)	Five mice
C57BL/6J: Substance P (1 μM)	Seven mice (30 vessels)	Four mice
C57BL/6J: CP-99994 (8 mM)	Seven mice (28 vessels)	Four mice
C57BL/6J: ML-133 (10 μM)	Five mice (36 vessels)	Four mice
C57BL/6J: BaCl$_2$ (100 μM)	Five mice (24 vessels)	Three mice

microscope. The position of the vessels imaged under the two-photon microscope relative to the cannula tip using the major surface vessels as landmarks.

Habituation

Mice were habituated to head-fixation on the spherical treadmill (60 mm diameter) over three days before imaging. Mice were habituated for 15 min of acclimation on the first day. On successive days, the time was increased to up to 2 hr for 3 to 4 days before imaging/electrophysiology/fiber photometry. During habituation, mice were monitored for any signs of distress. 2PLSM data were taken over four imaging sessions, with two sessions for each condition.

Intraperitoneal injections and cortical infusions

CNO (2.5 mg/kg in 2% DMSO in saline) or 2%DMSO in saline were injected intraperitoneal 20 min before imaging began. Pilot electrophysiological experiments showed that the effects of DREADDs on neural activity onset within 20 min of injection. Injections of CNO and DMSO were counterbalanced.

For the intracortical infusions, mice were first head-fixed on the spherical treadmill. The dummy cannula was then slowly removed and replaced with an infusion cannula (Plastics One, C315IS-4). The interface between the infusion cannula and the guide cannula was sealed with Kwik-Cast (World Precision Instruments). All infusions were done at a rate of 25 nL/min for a total volume of 500 nL. Animals were kept in place for 20 min after the end of the infusion and then moved to the imaging apparatus. The infusion cannulas were kept in place for the duration of the imaging session. Pharmacological treatments and aCSF were each infused in a counterbalanced order.

Physiological measurements

Two-photon microscopy

Prior to imaging, mice (n = 107 mice) were briefly anesthetized with isoflurane, and retro-orbitally injected with 50 μL 5% (weight/volume) fluorescein conjugated dextran (FITC-dextran 70 kDa; Sigma-Aldrich) (*Drew et al., 2011*; *Shih et al., 2012b*) then head-fixed upon a spherical treadmill. The treadmill was coated with anti-slip tape and attached to an optical rotary encoder (US Digital, E7PD-720–118) to monitor rotational of the treadmill. Imaging was done on a Sutter Movable Objective Microscope with a 16 × 0.8 NA objective (Nikon). A MaiTai HP laser (Spectra-Physics) tuned to 800 nm was used to excite the FITC. The power exiting the objective was 10–15 mW for imaging surface arteries. For vessel diameter measurements, movies of individual arteries were taken at a nominal frame rate of 8 Hz for 5 min. For RBC velocity measurements, line-scans were made along the long axis of the capillary lumen (Figure S4A) (*Drew et al., 2010a*). The same vessel segments were imaged after both the treatment (intraperitoneal CNO injection or local drug infusion) and vehicle controls (intraperitoneal vehicle injection or intracranial vehicle infusion). Treatments and vehicle condition were imaged in a counterbalanced order on separate days. Imaged arteries were chosen in the first session of imaging. Arteries were visually identified by their more rapid blood flow, rapid temporal dynamics of their response to locomotion, and vasomotion (*Drew et al., 2010b*; *Drew et al., 2011*; *Winder et al., 2017*). Bright field and fluorescent images of the PoRTs window were taken before imaging on the two-photon for each mouse. For imaging experiments with DREADDs manipulations, vessels were selected for imaging if they were within the region expressing fluorescent reporter protein (*Figure 2A*). For infusion imaging experiments, selected vessels were less than 1.5 mm from the cannula. For repeated imaging of the same vessel, three-dimensional image stacks of the regions were made, and the position of nearby vessels were used to return to the same imaging plane on subsequent imaging sessions. Vessels within the targeted region were chosen on the first (and third for DREADD experiments) imaging session randomly, and the analysis was done with automated software, effectively blinding the experimenter. Only vessels anatomically identified to be in the FL/HL representation were used in locomotion-triggered averages.

Image processing and data analysis

Data analysis was performed in MATLAB (MathWorks). 2PLSM images were aligned in the x–y plane using a rigid-body registration algorithm (*Drew et al., 2011*). Each movie was visually reviewed to ensure that z-axis motion during locomotion was minimal. For surface arteries, the intensity of a

short segment (1–3 µm in length) was averaged along the long axis of the vessel, and the diameter was calculated from the full-width at half-maximum (https://github.com/DrewLab/Surface-Vessel-FWHM-Diameter, *Drew et al., 2011*). For penetrating arteries, the Thresholding in Radon Space (TiRS) method was used as it effectively performs a full-width at half maximum measurement along every angle of the penetrating artery (https://github.com/DrewLab/Thresholding_in_Radon_Space, *Gao and Drew, 2014*). For diameters of penetrating vessels, using the TiRS method is important as penetrating vessels are not circular and the cross sectional shape will change during dilation, making single-axis diameter measurements inaccurate (*Greensmith and Duling, 1984*; *Steelman et al., 2010*; *Gao and Drew, 2014*). A square region of interest (ROI) enclosing the penetrating arteriole of interest was manually drawn. The images were transformed into Radon space, thresholded, and then transformed back to image space, where the vessel cross-sectional area was quantified after a second thresholding. In order to facilitate comparison with pial vessels, diameters (D) of penetrating vessels were taken to be: $D=2\sqrt{A/\pi}$, where A was the cross-sectional area calculated using the TiRS method. Frames in which the temporal derivative of diameter changed by >16 µm/s were tagged as motion artifacts and replaced with the linear interpolation between the proceeding and subsequent points. The diameter was filtered with a five-point median filter (MATLAB function: medfilt1; filter order = 5). Red blood cell velocity in capillaries was calculated using the Radon transform (*Drew et al., 2010a*) (https://github.com/DrewLab/MCS_Linescan). Example images of individual vessels were taken from movies that were 3D median filtered in ImageJ (ImageJ: 3D Median, radius = 2) (the third dimention here being time), and then the max intensity projection was taken for 40 frames with or without locomotion.

To detect locomotion events, the velocity signal from the rotational encoder on the spherical treadmill was low-pass filtered (10 Hz, fifth-order Butterworth), and then the absolute value of the acceleration was binarized with a 10^{-5} cm/s^2 threshold (*Huo et al., 2014*; *Huo et al., 2015b*). Stationary periods were defined as periods when the mouse was still, with at least a 2 s buffer after the end of any preceding locomotion event and a 1 s buffer before the start of the next locomotion event. Onset time was calculated by finding the time intercept of a line fit through the points in the locomotion-triggered average that were 20% and 80% of the peak dilation (*Tian et al., 2010*). The change in basal diameter in each treatment condition was normalized by the basal diameter of the same vessel in the vehicle control condition unless otherwise specified.

For the vessels that were histologically identified as being within the FL/HL representation, locomotion-triggered averages (LTA) were calculated by taking the average of any locomotion event >5 s in duration with at least 2 s of no locomotion before the event. These averages were normalized by the average basal diameter of the same vessel under vehicle control conditions.

Electrophysiology

Neural activity was recorded as differential potentials between the two leads of Teflon-insulated tungsten micro-wires (A-M Systems, #795500) (*Huo et al., 2014*; *Winder et al., 2017*). Differential recordings between two closely spaced electrodes avoid the volume conduction of remote signals (*Parabucki and Lampl, 2017*). Stereotrode micro-wires, with an inter-electrode spacing of ~100 µm, were threaded through polyimide tubing (A-M Systems, #822200). Electrode impedances were between 70 and 120 kΩ at 1 kHz. The electrodes were implanted in the upper layers of cortex (~400 µm depth). The acquired signals were amplified (World Precision Instruments, DAM80), band-pass filtered between 0.1 and 10 kHz (Brownlee Precision, Model 440) during acquisition, then digitized at 20 kHz.

Power was calculated after digitally band-pass filtering the raw neural signal (MATLAB function: butter, filtfilt; filter order = 4). The local field potential (LFP) was calculated by digitally band-pass filtering the raw neural signal between 10–100 Hz (MATLAB function: butter, filtfilt; filter order = 4) and using a notch filter to remove 60 Hz noise (MATLAB function: iirnotch). The basal power was computed by calculating the power during periods of no locomotion. The locomotion power was computed by calculating the power during periods of locomotion. Gamma-band power was quantified by averaging the 40–100 Hz band of the LFP after using a notch filter to remove 60 Hz noise.

Fiber photometry

Mice were injected with 0.5 µL of AAV with a GCaMP6s construct (AAV9-CaMKII-GCaMP6s-WPRE-Sv40 from Addgene, or AAV8-syn-GCaMP-WPRE or AAV8-FLEX-syn-GCaMP-WPRE from Vigene). After a month of recovery, mice underwent surgery to implant a titanium head bar and a fiber optic canula (1.5 mm length, 200 µm diameter, 0.48NA, Doric Lenses, Quebec, Canada) in the FL/HL representation. Two days later, the mice began habituation to being headfixed on the spherical treadmill of the same design used for two-photon imaging. Four days of habituation took place before any recordings were made. For fiber photometry measurements, we used a Doric Lenses system with LEDs illuminating at 405, 465, and 560 nm, and collected fluorescence between 500 and 540 nm (GFP or GCaMP) and 580–680 nm (TRITC) at 12 kHz which was then down-sampled to 1.2 kHz. Prior to measurements, mice were briefly anesthetized with isoflurane and 50 µL of 5% TRITC dextran (70kD, Sigma-Aldrich) was injected into the retroorbital sinus. Data was acquired starting 20 min after the injection. Data from each mouse was taken over three sessions (~2 hr each) with the Doric Neuroscience studio software.

Fluorescence correction and Z-scoring

All data processing was done in MATLAB. Locomotion data was zero-lag low-pass filtered below 10 Hz and then binarized into locomotion or not locomoting, using a threshold set based on the absolute value of the first derivative of the signal. To correct for excretion of TRITC and photobleaching of GCaMP signals, raw fluorescence signals were zero-lag low pass filtered below 0.1 Hz and periods of locomotion and the following fifteen seconds were excluded from the data set to avoid contamination of metabolic decay with behavior-evoked blood volume changes. This data was then fit with the sum of two exponential decays which was subsequently subtracted from the raw broadband signal. The corrected signals were then zero-lag low pass filtered below 1 Hz. To correct for variable signal intensities, low pass filtered signals were then normalized to have a minimum of 0 and maxima of 1. Because increases in local hemoglobin concentration attenuate GCaMP signals, correction of GCaMP signals with respect to the acquired blood volume signal was performed. Three animals expressing GFP ubiquitously (*Okabe et al., 1997*) were used to determine the relationship between changes in blood volume and the fluorescence signal. The relationship between the green fluorescence and CBV was modeled using a linear function and the slopes of the three animals were averaged to determine the mean attenuation coefficient. To correct the effect of CBV changes on GCaMP fluorescence, TRITC signal was multiplied by this coefficient and then subtracted from the GCaMP channel, removing any effects of increased hemoglobin on fluorescence. All GCaMP data was then zero-lag bandpass filtered between [0.001 Hz and 1 Hz]. Fluorescence intensity was then converted to z-scores. Locomotion events were defined as periods of locomotion at least 5 s in duration with at least 5 s preceding locomotion onset free of any behavior to establish resting baseline of hemodynamic and GCaMP signals. Locomotion events were separated in to five groups based on their duration for analysis, [5.0–9.99 s], [10–14.99 s], [15–29.99 s], [30.00–44.99 s], and [45.0s+]. A baseline of the average intensity preceding each locomotion event was subtracted from each event, and averages were calculated within each category.

Histology

At the end of the experiment, mice were deeply anesthetized with 5% isoflurane, and then transcardially perfused with heparinized saline followed by 4% paraformaldehyde. The brain was removed from the skull and sunk in 30% sucrose/4% PFA. For cytochrome oxidase staining, the cortex was then flattened and 60 µm tangential sections were cut on a freezing microtome. The cytochrome oxidase in the sections was stained, and the location of the FL/HL representation in somatosensory cortex was reconstructed relative to the vasculature visible through the cranial window (*Adams et al., 2018*).

For immunohistochemistry labeling, the brains were immersed in a 4% PFA/30% sucrose solution for 1 day. Tissues were sectioned coronally to a 90 µm thickness and then washed in PBS twice. For heat-induced antigen retrieval, the slices were boiled in 10 mM sodium citrate for 10 min. The sections were then incubated with primary antibodies on slides at a 1:200 dilution for two days at 4°C (Mouse monoclonal GAD-65 Antibody (A-3): sc-377145 Santa Cruz Biotechnology, Mouse monoclonal CaMKII Antibody (G-1): sc-5306 Santa Cruz Biotechnology, Rabbit polyclonal to GFAP: ab7260

abcam, Goat polyclonal anti-nNOS: ab1376 Abcam). The brain sections were washed twice and incubated for one hour with secondary antibodies (Abcam Alexa Fluor 488 Goat Anti-Mouse IgG H and L and Goat Anti-Rabbit IgG H and L). The brain sections were washed twice, and coverslipped with DAPI fluroshield mounting media (Abcam ab104139). The sections were imaged on an Olympus FV10i Confocal. Manual quantification of cell specificity were done in 318 µm x 318 µm x 120 µm volumes. Type 1 nNOS neurons were distinguished from type two neurons by their substantially more intense staining for nNOS (*Perrenoud et al., 2012*).

Statistical analysis

Statistical analysis was performed using MATLAB (R2018, MathWorks). All summary data were reported as mean ± standard deviation and plotted as mean ± standard error unless otherwise specified. For comparisons of vehicle vs. treatment conditions, where multiple measurements of different vessel diameters were taken from the same mouse, we used the linear mixed effects (LME) model (MATLAB function: fitlme). For each manipulation (e.g. CNO vs. vehicle in DREADD-expressing mice), we fit a linear mixed effects model given by:

$$D_{n,a} = \gamma + \beta_a$$

where $D_{n,a}$ is the diameter differences between the vehicle and manipulation condition, a is the identifier of the animal group, and n is the identifier of the vessel. The γ term is the (fixed) effect of the manipulation, and β_a is the within animal (random) effect that accounts for the within animal correlations (*Aarts et al., 2014*). To determine if the manipulation caused a significant change in the vessel diameter, we calculated if the γ term differed from 0, after a Bonferroni correction for the number of groups of DREADD-expressing mice (7 groups) or the number of infusions (6 groups). p-Values >1 after correction were rounded down to 1. A difference was determined to be statistically significant if p<0.05 after Bonferroni correction. For plotting the relationship of the basal diameter in the control condition versus the manipulation in the figures, we fit a linear mixed effects model given by:

$$D_{n,a} = \gamma + \beta_a + \alpha_n D_n$$

where D_n is the diameter of vessel n in the control condition, and α_n is a vector of (fixed) coefficients.

For comparisons of vehicle vs. treatment conditions of the gamma-band (averaged power from 40 to 100 Hz after removing 60 Hz noise), we used the paired t-test (MATLAB function: ttest).

Author contributions

Christina T Echagarruga, Conceptualization, Data curation, Software, Formal analysis, Investigation, Visualization, Methodology, Writing - original draft, Writing - review and editing; Kyle W Gheres, Conceptualization, Resources, Data curation, Software, Formal analysis, Validation, Investigation, Visualization, Methodology, Writing - original draft, Writing - review and editing; Jordan N Norwood, Funding acquisition, Investigation, Visualization, Writing - original draft; Patrick J Drew, Conceptualization, Software, Formal analysis, Supervision, Funding acquisition, Validation, Investigation, Visualization, Methodology, Writing - original draft, Project administration, Writing - review and editing

Author ORCIDs

Kyle W Gheres (iD) https://orcid.org/0000-0001-7568-9023
Jordan N Norwood (iD) http://orcid.org/0000-0001-8093-5938
Patrick J Drew (iD) https://orcid.org/0000-0002-7483-7378

Ethics

Animal experimentation: This study was performed in strict accordance with the recommendations in the Guide for the Care and Use of Laboratory Animals of the National Institutes of Health. All procedures were performed in accordance with protocols approved by the Institutional Animal Care and Use Committee (IACUC) of Pennsylvania State University (protocol # 201042827). All surgeries were performed under isoflurane anesthesia and every effort was made to minimize suffering.

Decision letter and Author response

Decision letter https://doi.org/10.7554/eLife.60533.sa1
Author response https://doi.org/10.7554/eLife.60533.sa2

Additional files

Supplementary files

• Transparent reporting form

Data availability

The Matlab code and data to generate the figures have been uploaded to Dryad. The DOI for download is here: https://doi.org/10.5061/dryad.b8gtht79h.

The following dataset was generated:

Author(s)	Year	Dataset title	Dataset URL	Database and Identifier
Echagarruga CT, Gheres K, Norwood JN, Drew PJ	2020	Data from: nNOS-expressing interneurons control basal and behaviorally-evoked arterial dilation in somatosensory cortex of mice	https://doi.org/10.5061/dryad.b8gtht79h	Dryad Digital Repository, 10.5061/dryad.b8gtht79h

References

Aarts E, Verhage M, Veenvliet JV, Dolan CV, van der Sluis S. 2014. A solution to dependency: using multilevel analysis to accommodate nested data. *Nature Neuroscience* **17**:491–496. DOI: https://doi.org/10.1038/nn.3648, PMID: 24671065

Abbott LF, Varela JA, Sen K, Nelson SB. 1997. Synaptic depression and cortical gain control. *Science* **275**:221–224. DOI: https://doi.org/10.1126/science.275.5297.221

Abbott NJ, Pizzo ME, Preston JE, Janigro D, Thorne RG. 2018. The role of brain barriers in fluid movement in the CNS: is there a 'glymphatic' system? *Acta Neuropathologica* **135**:387–407. DOI: https://doi.org/10.1007/s00401-018-1812-4, PMID: 29428972

Adachi K, Takahashi S, Melzer P, Campos KL, Nelson T, Kennedy C, Sokoloff L. 1994. Increases in local cerebral blood flow associated with somatosensory activation are not mediated by NO. *American Journal of Physiology-Heart and Circulatory Physiology* **267**:H2155–H2162. DOI: https://doi.org/10.1152/ajpheart.1994.267.6.H2155

Adams MD, Winder AT, Blinder P, Drew PJ. 2018. The pial vasculature of the mouse develops according to a sensory-independent program. *Scientific Reports* **8**:9860. DOI: https://doi.org/10.1038/s41598-018-27910-3, PMID: 29959346

Adebiyi A, Zhao G, Cheranov SY, Ahmed A, Jaggar JH. 2007. Caveolin-1 abolishment attenuates the myogenic response in murine cerebral arteries. *American Journal of Physiology-Heart and Circulatory Physiology* **292**: H1584–H1592. DOI: https://doi.org/10.1152/ajpheart.00584.2006, PMID: 17098833

Alagem N, Dvir M, Reuveny E. 2001. Mechanism of $^{ba(2+)}$) block of a mouse inwardly rectifying K$^+$ channel: differential contribution by two discrete residues. *The Journal of Physiology* **534**:381–393. DOI: https://doi.org/10.1111/j.1469-7793.2001.00381.x, PMID: 11454958

Alexander GM, Rogan SC, Abbas AI, Armbruster BN, Pei Y, Allen JA, Nonneman RJ, Hartmann J, Moy SS, Nicolelis MA, McNamara JO, Roth BL. 2009. Remote control of neuronal activity in transgenic mice expressing evolved G protein-coupled receptors. *Neuron* **63**:27–39. DOI: https://doi.org/10.1016/j.neuron.2009.06.014, PMID: 19607790

Amarillo Y, Zagha E, Mato G, Rudy B, Nadal MS. 2014. The interplay of seven subthreshold conductances controls the resting membrane potential and the oscillatory behavior of thalamocortical neurons. *Journal of Neurophysiology* **112**:393–410. DOI: https://doi.org/10.1152/jn.00647.2013, PMID: 24760784

Anenberg E, Chan AW, Xie Y, LeDue JM, Murphy TH. 2015. Optogenetic stimulation of GABA neurons can decrease local neuronal activity while increasing cortical blood flow. *Journal of Cerebral Blood Flow & Metabolism* **35**:1579–1586. DOI: https://doi.org/10.1038/jcbfm.2015.140, PMID: 26082013

Atochin DN, Huang PL. 2011. Role of endothelial nitric oxide in cerebrovascular regulation. *Current Pharmaceutical Biotechnology* **12**:1334–1342. DOI: https://doi.org/10.2174/138920111798280974, PMID: 21235451

Attwell D, Buchan AM, Charpak S, Lauritzen M, Macvicar BA, Newman EA. 2010. Glial and neuronal control of brain blood flow. *Nature* **468**:232–243. DOI: https://doi.org/10.1038/nature09613, PMID: 21068832

Augustine V, Gokce SK, Lee S, Wang B, Davidson TJ, Reimann F, Gribble F, Deisseroth K, Lois C, Oka Y. 2018. Hierarchical neural architecture underlying thirst regulation. *Nature* **555**:204–209. DOI: https://doi.org/10.1038/nature25488, PMID: 29489747

Aydin AK, Haselden WD, Goulam Houssen Y, Pouzat C, Rungta RL, Demené C, Tanter M, Drew PJ, Charpak S, Boido D. 2020. Transfer functions linking neural calcium to single voxel functional ultrasound signal. *Nature Communications* **11**:2954. DOI: https://doi.org/10.1038/s41467-020-16774-9, PMID: 32528069

Bagher P, Segal SS. 2011. Regulation of blood flow in the microcirculation: role of conducted vasodilation. *Acta Physiologica* **202**:271–284. DOI: https://doi.org/10.1111/j.1748-1716.2010.02244.x, PMID: 21199397

Barbaresi P, Mensà E, Lariccia V, Desiato G, Fabri M, Gratteri S. 2015. Intracallosal neuronal nitric oxide synthase neurons colocalize with neurokinin 1 substance P receptor in the rat. *Journal of Comparative Neurology* **523**: 589–607. DOI: https://doi.org/10.1002/cne.23695, PMID: 25312245

Bazargani N, Attwell D. 2016. Astrocyte calcium signaling: the third wave. *Nature Neuroscience* **19**:182–189. DOI: https://doi.org/10.1038/nn.4201, PMID: 26814587

Beloozerova IN, Sirota MG. 1993. The role of the motor cortex in the control of accuracy of locomotor movements in the cat. *The Journal of Physiology* **461**:1–25. DOI: https://doi.org/10.1113/jphysiol.1993.sp019498, PMID: 8350259

Bland-Ward PA, Moore PK. 1995. 7-Nitro indazole derivatives are potent inhibitors of brain, endothelium and inducible isoforms of nitric oxide synthase. *Life Sciences* **57**:PL131–PL135. DOI: https://doi.org/10.1016/0024-3205(95)02046-L, PMID: 7544863

Blottner D, Grozdanovic Z, Gossrau R. 1995. Histochemistry of nitric oxide synthase in the nervous system. *The Histochemical Journal* **27**:785–811. DOI: https://doi.org/10.1007/BF02388304, PMID: 8575942

Bonder DE, McCarthy KD. 2014. Astrocytic Gq-GPCR-linked IP3R-dependent Ca2+ signaling does not mediate neurovascular coupling in mouse visual cortex in vivo. *Journal of Neuroscience* **34**:13139–13150. DOI: https://doi.org/10.1523/JNEUROSCI.2591-14.2014, PMID: 25253859

Boynton GM. 2011. Spikes, BOLD, attention, and awareness: a comparison of electrophysiological and fMRI signals in V1. *Journal of Vision* **11**:12. DOI: https://doi.org/10.1167/11.5.12, PMID: 22199162

Cardoso MM, Sirotin YB, Lima B, Glushenkova E, Das A. 2012. The neuroimaging signal is a linear sum of neurally distinct stimulus- and task-related components. *Nature Neuroscience* **15**:1298–1306. DOI: https://doi.org/10.1038/nn.3170, PMID: 22842146

Cardoso MMB, Lima B, Sirotin YB, Das A. 2019. Task-related hemodynamic responses are modulated by reward and task engagement. *PLOS Biology* **17**:e3000080. DOI: https://doi.org/10.1371/journal.pbio.3000080, PMID: 31002659

Cauli B, Tong XK, Rancillac A, Serluca N, Lambolez B, Rossier J, Hamel E. 2004. Cortical GABA interneurons in neurovascular coupling: relays for subcortical vasoactive pathways. *Journal of Neuroscience* **24**:8940–8949. DOI: https://doi.org/10.1523/JNEUROSCI.3065-04.2004, PMID: 15483113

Cauli B, Hamel E. 2010. Revisiting the role of neurons in neurovascular coupling. *Frontiers in Neuroenergetics* **2**: 9. DOI: https://doi.org/10.3389/fnene.2010.00009, PMID: 20616884

Cerri D, Albaugh D, Katz B, Lee S, Walton LR, Zhang W, Etkin A, Cui G, Stuber G, Shih YY. 2019. Mechanisms underlying negative fMRI responses in the striatum. *Journal of Cerebral Blood Flow & Metabolism* **39**: X19850985. DOI: https://doi.org/10.1177/0271678X19850985

Chaigneau E, Oheim M, Audinat E, Charpak S. 2003. Two-photon imaging of capillary blood flow in olfactory bulb glomeruli. *PNAS* **100**:13081–13086. DOI: https://doi.org/10.1073/pnas.2133652100, PMID: 14569029

Chapin JK, Waterhouse BD, Woodward DJ. 1981. Differences in cutaneous sensory response properties of single somatosensory cortical neurons in awake and halothane anesthetized rats. *Brain Research Bulletin* **6**:63–70. DOI: https://doi.org/10.1016/S0361-9230(81)80069-X, PMID: 6258757

Chapin JK, Lin CS. 1984. Mapping the body representation in the SI cortex of anesthetized and awake rats. *The Journal of Comparative Neurology* **229**:199–213. DOI: https://doi.org/10.1002/cne.902290206, PMID: 6438190

Chapin JK, Woodward DJ. 1981. Modulation of sensory responsiveness of single somatosensory cortical cells during movement and arousal behaviors. *Experimental Neurology* **72**:164–178. DOI: https://doi.org/10.1016/0014-4886(81)90135-7, PMID: 7202621

Chapin JK, Woodward DJ. 1982. Somatic sensory transmission to the cortex during movement: phasic modulation over the locomotor step cycle. *Experimental Neurology* **78**:670–684. DOI: https://doi.org/10.1016/0014-4886(82)90083-8

Chen BR, Bouchard MB, McCaslin AF, Burgess SA, Hillman EM. 2011. High-speed vascular dynamics of the hemodynamic response. *NeuroImage* **54**:1021–1030. DOI: https://doi.org/10.1016/j.neuroimage.2010.09.036, PMID: 20858545

Chen TW, Wardill TJ, Sun Y, Pulver SR, Renninger SL, Baohan A, Schreiter ER, Kerr RA, Orger MB, Jayaraman V, Looger LL, Svoboda K, Kim DS. 2013. Ultrasensitive fluorescent proteins for imaging neuronal activity. *Nature* **499**:295–300. DOI: https://doi.org/10.1038/nature12354, PMID: 23868258

Cohen ER, Ugurbil K, Kim SG. 2002. Effect of basal conditions on the magnitude and dynamics of the blood oxygenation level-dependent fMRI response. *Journal of Cerebral Blood Flow & Metabolism* **22**:1042–1053. DOI: https://doi.org/10.1097/00004647-200209000-00002, PMID: 12218410

Cooke SF, Komorowski RW, Kaplan ES, Gavornik JP, Bear MF. 2015. Visual recognition memory, manifested as long-term habituation, requires synaptic plasticity in V1. *Nature Neuroscience* **18**:262–271. DOI: https://doi.org/10.1038/nn.3920, PMID: 25599221

Cudmore RH, Dougherty SE, Linden DJ. 2017. Cerebral vascular structure in the motor cortex of adult mice is stable and is not altered by voluntary exercise. *Journal of Cerebral Blood Flow & Metabolism* **37**:3725–3743. DOI: https://doi.org/10.1177/0271678X16682508, PMID: 28059584

D'Esposito M, Deouell LY, Gazzaley A. 2003. Alterations in the BOLD fMRI signal with ageing and disease: a challenge for neuroimaging. *Nature Reviews Neuroscience* **4**:863–872. DOI: https://doi.org/10.1038/nrn1246, PMID: 14595398

Dittrich L, Heiss JE, Warrier DR, Perez XA, Quik M, Kilduff TS. 2012. Cortical nNOS neurons co-express the NK1 receptor and are depolarized by substance P in multiple mammalian species. *Frontiers in Neural Circuits* **6**:31. DOI: https://doi.org/10.3389/fncir.2012.00031, PMID: 22679419

Dittrich L, Morairty SR, Warrier DR, Kilduff TS. 2015. Homeostatic sleep pressure is the primary factor for activation of cortical nNOS/NK1 neurons. *Neuropsychopharmacology* **40**:632–639. DOI: https://doi.org/10.1038/npp.2014.212, PMID: 25139062

Drew PJ, Duyn JH, Golanov E, Kleinfeld D. 2008. Finding coherence in spontaneous oscillations. *Nature Neuroscience* **11**:991–993. DOI: https://doi.org/10.1038/nn0908-991, PMID: 18725901

Drew PJ, Blinder P, Cauwenberghs G, Shih AY, Kleinfeld D. 2010a. Rapid determination of particle velocity from space-time images using the radon transform. *Journal of Computational Neuroscience* **29**:5–11. DOI: https://doi.org/10.1007/s10827-009-0159-1, PMID: 19459038

Drew PJ, Shih AY, Driscoll JD, Knutsen PM, Blinder P, Davalos D, Akassoglou K, Tsai PS, Kleinfeld D. 2010b. Chronic optical access through a polished and reinforced thinned skull. *Nature Methods* **7**:981–984. DOI: https://doi.org/10.1038/nmeth.1530, PMID: 20966916

Drew PJ, Shih AY, Kleinfeld D. 2011. Fluctuating and sensory-induced vasodynamics in rodent cortex extend arteriole capacity. *PNAS* **108**:8473–8478. DOI: https://doi.org/10.1073/pnas.1100428108, PMID: 21536897

Drew PJ. 2019. Vascular and neural basis of the BOLD signal. *Current Opinion in Neurobiology* **58**:61–69. DOI: https://doi.org/10.1016/j.conb.2019.06.004, PMID: 31336326

Drew PJ, Winder AT, Zhang Q. 2019. Twitches, blinks, and fidgets: important generators of ongoing neural activity. *The Neuroscientist* **25**:298–313. DOI: https://doi.org/10.1177/1073858418805427, PMID: 30311838

Drew PJ, Mateo C, Turner KL, Yu X, Kleinfeld D. 2020. Ultra-slow oscillations in fMRI and Resting-State connectivity: neuronal and vascular contributions and technical confounds. *Neuron* **107**:782–804. DOI: https://doi.org/10.1016/j.neuron.2020.07.020, PMID: 32791040

Dun NJ, Huang R, Dun SL, Förstermann U. 1994. Infrequent co-localization of nitric oxide synthase and calcium binding proteins immunoreactivity in rat neocortical neurons. *Brain Research* **666**:289–294. DOI: https://doi.org/10.1016/0006-8993(94)90786-2, PMID: 7533636

Eftekhari S, Westgate CSJ, Johansen KP, Bruun SR, Jensen RH. 2020. Long-term monitoring of intracranial pressure in freely-moving rats; impact of different physiological states. *Fluids and Barriers of the CNS* **17**:39. DOI: https://doi.org/10.1186/s12987-020-00199-z, PMID: 32517699

Egger V, Stroh O. 2009. Calcium buffering in rodent olfactory bulb granule cells and mitral cells. *The Journal of Physiology* **587**:4467–4479. DOI: https://doi.org/10.1113/jphysiol.2009.174540, PMID: 19635818

Einevoll GT, Kayser C, Logothetis NK, Panzeri S. 2013. Modelling and analysis of local field potentials for studying the function of cortical circuits. *Nature Reviews Neuroscience* **14**:770–785. DOI: https://doi.org/10.1038/nrn3599, PMID: 24135696

Endo T, Yanagawa Y, Komatsu Y. 2016. Substance P activates Ca2+-Permeable nonselective cation channels through a Phosphatidylcholine-Specific phospholipase C signaling pathway in nNOS-Expressing GABAergic neurons in visual cortex. *Cerebral Cortex* **26**:669–682. DOI: https://doi.org/10.1093/cercor/bhu233, PMID: 25316339

Engelhardt T, Lowe PR, Galley HF, Webster NR. 2006. Inhibition of neuronal nitric oxide synthase reduces the propofol requirements in wild-type and nNOS knockout mice. *European Journal of Anaesthesiology* **23**:197–201. DOI: https://doi.org/10.1017/S0265021505002188, PMID: 16430790

Ferezou I, Bolea S, Petersen CC. 2006. Visualizing the cortical representation of whisker touch: voltage-sensitive dye imaging in freely moving mice. *Neuron* **50**:617–629. DOI: https://doi.org/10.1016/j.neuron.2006.03.043, PMID: 16701211

Fung YC, Zweifach BW, Intaglietta M. 1966. Elastic environment of the capillary bed. *Circulation Research* **19**: 441–461. DOI: https://doi.org/10.1161/01.RES.19.2.441, PMID: 5914856

Gagnon L, Sakadžić S, Lesage F, Musacchia JJ, Lefebvre J, Fang Q, Yücel MA, Evans KC, Mandeville ET, Cohen-Adad J, Polimeni JR, Yaseen MA, Lo EH, Greve DN, Buxton RB, Dale AM, Devor A, Boas DA. 2015. Quantifying the microvascular origin of BOLD-fMRI from first principles with two-photon microscopy and an oxygen-sensitive nanoprobe. *Journal of Neuroscience* **35**:3663–3675. DOI: https://doi.org/10.1523/JNEUROSCI.3555-14.2015, PMID: 25716864

Gao YR, Greene SE, Drew PJ. 2015. Mechanical restriction of intracortical vessel dilation by brain tissue sculpts the hemodynamic response. *NeuroImage* **115**:162–176. DOI: https://doi.org/10.1016/j.neuroimage.2015.04.054, PMID: 25953632

Gao YR, Ma Y, Zhang Q, Winder AT, Liang Z, Antinori L, Drew PJ, Zhang N. 2017. Time to wake up: studying neurovascular coupling and brain-wide circuit function in the un-anesthetized animal. *NeuroImage* **153**:382–398. DOI: https://doi.org/10.1016/j.neuroimage.2016.11.069, PMID: 27908788

Gao YR, Drew PJ. 2014. Determination of vessel cross-sectional area by thresholding in radon space. *Journal of Cerebral Blood Flow & Metabolism* **34**:1180–1187. DOI: https://doi.org/10.1038/jcbfm.2014.67, PMID: 24736890

Gao YR, Drew PJ. 2016. Effects of voluntary locomotion and calcitonin Gene-Related peptide on the dynamics of single dural vessels in awake mice. *The Journal of Neuroscience* **36**:2503–2516. DOI: https://doi.org/10.1523/JNEUROSCI.3665-15.2016, PMID: 26911696

Garthwaite J. 2008. Concepts of neural nitric oxide-mediated transmission. *European Journal of Neuroscience* **27**:2783–2802. DOI: https://doi.org/10.1111/j.1460-9568.2008.06285.x, PMID: 18588525

Gehrmann J, Hammer PE, Maguire CT, Wakimoto H, Triedman JK, Berul CI. 2000. Phenotypic screening for heart rate variability in the mouse. *American Journal of Physiology-Heart and Circulatory Physiology* **279**:H733–H740. DOI: https://doi.org/10.1152/ajpheart.2000.279.2.H733, PMID: 10924073

Gerashchenko D, Wisor JP, Burns D, Reh RK, Shiromani PJ, Sakurai T, de la Iglesia HO, Kilduff TS. 2008. Identification of a population of sleep-active cerebral cortex neurons. *PNAS* **105**:10227–10232. DOI: https://doi.org/10.1073/pnas.0803125105, PMID: 18645184

Goense JB, Logothetis NK. 2008. Neurophysiology of the BOLD fMRI signal in awake monkeys. *Current Biology* **18**:631–640. DOI: https://doi.org/10.1016/j.cub.2008.03.054, PMID: 18439825

Goriely A, Geers MG, Holzapfel GA, Jayamohan J, Jérusalem A, Sivaloganathan S, Squier W, van Dommelen JA, Waters S, Kuhl E. 2015. Mechanics of the brain: perspectives, challenges, and opportunities. *Biomechanics and Modeling in Mechanobiology* **14**:931–965. DOI: https://doi.org/10.1007/s10237-015-0662-4, PMID: 25716305

Gould IG, Tsai P, Kleinfeld D, Linninger A. 2017. The capillary bed offers the largest hemodynamic resistance to the cortical blood supply. *Journal of Cerebral Blood Flow & Metabolism* **37**:52–68. DOI: https://doi.org/10.1177/0271678X16671146, PMID: 27780904

Greenberg JH, Hamada J, Rysman K. 1997. Distribution of N(omega)-nitro-L-arginine following topical and intracerebroventricular administration in the rat. *Neuroscience Letters* **229**:1–4. DOI: https://doi.org/10.1016/S0304-3940(97)00395-9, PMID: 9224787

Greensmith JE, Duling BR. 1984. Morphology of the constricted arteriolar wall: physiological implications. *American Journal of Physiology-Heart and Circulatory Physiology* **247**:H687–H698. DOI: https://doi.org/10.1152/ajpheart.1984.247.5.H687, PMID: 6496751

Gunaydin LA, Grosenick L, Finkelstein JC, Kauvar IV, Fenno LE, Adhikari A, Lammel S, Mirzabekov JJ, Airan RD, Zalocusky KA, Tye KM, Anikeeva P, Malenka RC, Deisseroth K. 2014. Natural neural projection dynamics underlying social behavior. *Cell* **157**:1535–1551. DOI: https://doi.org/10.1016/j.cell.2014.05.017, PMID: 24949967

Hald BO, Jensen LJ, Sørensen PG, Holstein-Rathlou NH, Jacobsen JC. 2012. Applicability of cable theory to vascular conducted responses. *Biophysical Journal* **102**:1352–1362. DOI: https://doi.org/10.1016/j.bpj.2012.01.055, PMID: 22455918

Hall CN, Reynell C, Gesslein B, Hamilton NB, Mishra A, Sutherland BA, O'Farrell FM, Buchan AM, Lauritzen M, Attwell D. 2014. Capillary pericytes regulate cerebral blood flow in health and disease. *Nature* **508**:55–60. DOI: https://doi.org/10.1038/nature13165, PMID: 24670647

Han K, Min J, Lee M, Kang BM, Park T, Hahn J, Yei J, Lee J, Woo J, Lee CJ, Kim SG, Suh M. 2019a. Neurovascular coupling under chronic stress is modified by altered GABAergic interneuron activity. *The Journal of Neuroscience* **39**:10081–10095. DOI: https://doi.org/10.1523/JNEUROSCI.1357-19.2019, PMID: 31672788

Han S, Miller JE, Byun S, Kim D, Risacher SL, Saykin AJ, Lee Y, Nho K, for Alzheimer's Disease Neuroimaging Initiative. 2019b. Identification of exon skipping events associated with Alzheimer's disease in the human hippocampus. *BMC Medical Genomics* **12**:13. DOI: https://doi.org/10.1186/s12920-018-0453-8, PMID: 30704480

Harnett MT, Xu NL, Magee JC, Williams SR. 2013. Potassium channels control the interaction between active dendritic integration compartments in layer 5 cortical pyramidal neurons. *Neuron* **79**:516–529. DOI: https://doi.org/10.1016/j.neuron.2013.06.005, PMID: 23931999

Harris KD, Quiroga RQ, Freeman J, Smith SL. 2016. Improving data quality in neuronal population recordings. *Nature Neuroscience* **19**:1165–1174. DOI: https://doi.org/10.1038/nn.4365, PMID: 27571195

Harrison TC, Pinto L, Brock JR, Dan Y. 2016. Calcium imaging of basal forebrain activity during innate and learned behaviors. *Frontiers in Neural Circuits* **10**:36. DOI: https://doi.org/10.3389/fncir.2016.00036, PMID: 27242444

Hartmann DA, Underly RG, Grant RI, Watson AN, Lindner V, Shih AY. 2015. Pericyte structure and distribution in the cerebral cortex revealed by high-resolution imaging of transgenic mice. *Neurophotonics* **2**:041402. DOI: https://doi.org/10.1117/1.NPh.2.4.041402, PMID: 26158016

Haselden WD, Kedarasetti RT, Drew PJ. 2020. Spatial and temporal patterns of nitric oxide diffusion and degradation drive emergent cerebrovascular dynamics. *PLOS Computational Biology* **16**:e1008069. DOI: https://doi.org/10.1371/journal.pcbi.1008069, PMID: 32716940

Hatashita S, Hoff JT. 1987. The effect of craniectomy on the biomechanics of normal brain. *Journal of Neurosurgery* **67**:573–578. DOI: https://doi.org/10.3171/jns.1987.67.4.0573, PMID: 3655895

Higley MJ, Sabatini BL. 2008. Calcium signaling in dendrites and spines: practical and functional considerations. *Neuron* **59**:902–913. DOI: https://doi.org/10.1016/j.neuron.2008.08.020, PMID: 18817730

Hill RA, Tong L, Yuan P, Murikinati S, Gupta S, Grutzendler J. 2015. Regional blood flow in the normal and ischemic brain is controlled by arteriolar smooth muscle cell contractility and not by capillary pericytes. *Neuron* **87**:95–110. DOI: https://doi.org/10.1016/j.neuron.2015.06.001, PMID: 26119027

Hillman EM. 2014. Coupling mechanism and significance of the BOLD signal: a status report. *Annual Review of Neuroscience* **37**:161–181. DOI: https://doi.org/10.1146/annurev-neuro-071013-014111, PMID: 25032494

Hosford PS, Gourine AV. 2019. What is the key mediator of the neurovascular coupling response? *Neuroscience & Biobehavioral Reviews* **96**:174–181. DOI: https://doi.org/10.1016/j.neubiorev.2018.11.011, PMID: 30481531

Huo BX, Smith JB, Drew PJ. 2014. Neurovascular coupling and decoupling in the cortex during voluntary locomotion. *Journal of Neuroscience* **34**:10975–10981. DOI: https://doi.org/10.1523/JNEUROSCI.1369-14.2014, PMID: 25122897

Huo BX, Greene SE, Drew PJ. 2015a. Venous cerebral blood volume increase during voluntary locomotion reflects cardiovascular changes. *NeuroImage* **118**:301–312. DOI: https://doi.org/10.1016/j.neuroimage.2015.06.011, PMID: 26057593

Huo BX, Gao YR, Drew PJ. 2015b. Quantitative separation of arterial and venous cerebral blood volume increases during voluntary locomotion. *NeuroImage* **105**:369–379. DOI: https://doi.org/10.1016/j.neuroimage.2014.10.030, PMID: 25467301

Hutchinson EB, Stefanovic B, Koretsky AP, Silva AC. 2006. Spatial flow-volume dissociation of the cerebral microcirculatory response to mild hypercapnia. *NeuroImage* **32**:520–530. DOI: https://doi.org/10.1016/j.neuroimage.2006.03.033, PMID: 16713717

Iadecola C. 1992. Nitric oxide participates in the cerebrovasodilation elicited from cerebellar fastigial nucleus. *American Journal of Physiology-Regulatory, Integrative and Comparative Physiology* **263**:R1156–R1161. DOI: https://doi.org/10.1152/ajpregu.1992.263.5.R1156, PMID: 1443234

Iadecola C. 2017. The neurovascular unit coming of age: a journey through neurovascular coupling in health and disease. *Neuron* **96**:17–42. DOI: https://doi.org/10.1016/j.neuron.2017.07.030, PMID: 28957666

Iliff JJ, Wang M, Liao Y, Plogg BA, Peng W, Gundersen GA, Benveniste H, Vates GE, Deane R, Goldman SA, Nagelhus EA, Nedergaard M. 2012. A paravascular pathway facilitates CSF flow through the brain parenchyma and the clearance of interstitial solutes, including amyloid β. *Science Translational Medicine* **4**:147ra111. DOI: https://doi.org/10.1126/scitranslmed.3003748, PMID: 22896675

Kawaguchi Y, Kubota Y. 1997. GABAergic cell subtypes and their synaptic connections in rat frontal cortex. *Cerebral Cortex* **7**:476–486. DOI: https://doi.org/10.1093/cercor/7.6.476, PMID: 9276173

Kedarasetti RT, Turner KL, Echagarruga C, Gluckman BJ, Drew PJ, Costanzo F. 2020. Functional hyperemia drives fluid exchange in the paravascular space. *Fluids and Barriers of the CNS* **17**:52. DOI: https://doi.org/10.1186/s12987-020-00214-3, PMID: 32819402

Kilduff TS, Cauli B, Gerashchenko D. 2011. Activation of cortical interneurons during sleep: an anatomical link to homeostatic sleep regulation? *Trends in Neurosciences* **34**:10–19. DOI: https://doi.org/10.1016/j.tins.2010.09.005, PMID: 21030095

Kim T, Hendrich KS, Masamoto K, Kim SG. 2007. Arterial versus total blood volume changes during neural activity-induced cerebral blood flow change: implication for BOLD fMRI. *Journal of Cerebral Blood Flow & Metabolism* **27**:1235–1247. DOI: https://doi.org/10.1038/sj.jcbfm.9600429, PMID: 17180136

Kim KJ, Ramiro Diaz J, Iddings JA, Filosa JA. 2016. Vasculo-Neuronal coupling: retrograde vascular communication to brain neurons. *The Journal of Neuroscience* **36**:12624–12639. DOI: https://doi.org/10.1523/JNEUROSCI.1300-16.2016, PMID: 27821575

Kim JH, Taylor AJ, Wang DJ, Zou X, Ress D. 2020. Dynamics of the cerebral blood flow response to brief neural activity in human visual cortex. *Journal of Cerebral Blood Flow & Metabolism* **40**:1823–1837. DOI: https://doi.org/10.1177/0271678X19869034, PMID: 31429358

Kim T, Kim SG. 2010. Cortical layer-dependent arterial blood volume changes: improved spatial specificity relative to BOLD fMRI. *NeuroImage* **49**:1340–1349. DOI: https://doi.org/10.1016/j.neuroimage.2009.09.061, PMID: 19800013

Kim SG, Ogawa S. 2012. Biophysical and physiological origins of blood oxygenation level-dependent fMRI signals. *Journal of Cerebral Blood Flow & Metabolism* **32**:1188–1206. DOI: https://doi.org/10.1038/jcbfm.2012.23, PMID: 22395207

Kleinfeld D, Mitra PP, Helmchen F, Denk W. 1998. Fluctuations and stimulus-induced changes in blood flow observed in individual capillaries in layers 2 through 4 of rat neocortex. *PNAS* **95**:15741–15746. DOI: https://doi.org/10.1073/pnas.95.26.15741, PMID: 9861040

Kleinfeld D, Blinder P, Drew PJ, Driscoll JD, Muller A, Tsai PS, Shih AY. 2011. A guide to delineate the logic of neurovascular signaling in the brain. *Frontiers in Neuroenergetics* **3**:1. DOI: https://doi.org/10.3389/fnene.2011.00001, PMID: 21559095

Krawchuk MB, Ruff CF, Yang X, Ross SE, Vazquez AL. 2020. Optogenetic assessment of VIP, PV, SOM and NOS inhibitory neuron activity and cerebral blood flow regulation in mouse somato-sensory cortex. *Journal of Cerebral Blood Flow & Metabolism* **40**:1427–1440. DOI: https://doi.org/10.1177/0271678X19870105, PMID: 31418628

Kubota Y, Shigematsu N, Karube F, Sekigawa A, Kato S, Yamaguchi N, Hirai Y, Morishima M, Kawaguchi Y. 2011. Selective coexpression of multiple chemical markers defines discrete populations of neocortical GABAergic neurons. *Cerebral Cortex* **21**:1803–1817. DOI: https://doi.org/10.1093/cercor/bhq252, PMID: 21220766

Lacroix A, Toussay X, Anenberg E, Lecrux C, Ferreirós N, Karagiannis A, Plaisier F, Chausson P, Jarlier F, Burgess SA, Hillman EM, Tegeder I, Murphy TH, Hamel E, Cauli B. 2015. COX-2-Derived prostaglandin E2 produced by pyramidal neurons contributes to neurovascular coupling in the rodent cerebral cortex. *Journal of Neuroscience* **35**:11791–11810. DOI: https://doi.org/10.1523/JNEUROSCI.0651-15.2015, PMID: 26311764

Lee SH, Rosenmund C, Schwaller B, Neher E. 2000. Differences in Ca^{2+} buffering properties between excitatory and inhibitory hippocampal neurons from the rat. *The Journal of Physiology* **525 Pt 2**:405–418. DOI: https://doi.org/10.1111/j.1469-7793.2000.t01-3-00405.x, PMID: 10835043

Lee SP, Duong TQ, Yang G, Iadecola C, Kim SG. 2001. Relative changes of cerebral arterial and venous blood volumes during increased cerebral blood flow: implications for BOLD fMRI. *Magnetic Resonance in Medicine* **45**:791–800. DOI: https://doi.org/10.1002/mrm.1107, PMID: 11323805

Lee L, Boorman L, Glendenning E, Christmas C, Sharp P, Redgrave P, Shabir O, Bracci E, Berwick J, Howarth C. 2020. Key aspects of neurovascular control mediated by specific populations of inhibitory cortical interneurons. *Cerebral Cortex* **30**:2452–2464. DOI: https://doi.org/10.1093/cercor/bhz251, PMID: 31746324

Lein ES, Hawrylycz MJ, Ao N, Ayres M, Bensinger A, Bernard A, Boe AF, Boguski MS, Brockway KS, Byrnes EJ, Chen L, Chen L, Chen TM, Chin MC, Chong J, Crook BE, Czaplinska A, Dang CN, Datta S, Dee NR, et al. 2007. Genome-wide atlas of gene expression in the adult mouse brain. *Nature* **445**:168–176. DOI: https://doi.org/10.1038/nature05453, PMID: 17151600

Leshan RL, Greenwald-Yarnell M, Patterson CM, Gonzalez IE, Myers MG. 2012. Leptin action through hypothalamic nitric oxide synthase-1–expressing neurons controls energy balance. *Nature Medicine* **18**:820–823. DOI: https://doi.org/10.1038/nm.2724, PMID: 22522563

Lindauer U, Megow D, Matsuda H, Dirnagl U. 1999. Nitric oxide: a modulator, but not a mediator, of neurovascular coupling in rat somatosensory cortex. *American Journal of Physiology-Heart and Circulatory Physiology* **277**:H799–H811. DOI: https://doi.org/10.1152/ajpheart.1999.277.2.H799, PMID: 10444508

Lindén H, Tetzlaff T, Potjans TC, Pettersen KH, Grün S, Diesmann M, Einevoll GT. 2011. Modeling the spatial reach of the LFP. *Neuron* **72**:859–872. DOI: https://doi.org/10.1016/j.neuron.2011.11.006, PMID: 22153380

Liu Y, Dang C, Garcia M, Gregersen H, Kassab GS. 2007. Surrounding tissues affect the passive mechanics of the vessel wall: theory and experiment. *American Journal of Physiology-Heart and Circulatory Physiology* **293**:H3290–H3300. DOI: https://doi.org/10.1152/ajpheart.00666.2007, PMID: 17873018

Logothetis NK. 2008. What we can do and what we cannot do with fMRI. *Nature* **453**:869–878. DOI: https://doi.org/10.1038/nature06976, PMID: 18548064

Longden TA, Dabertrand F, Koide M, Gonzales AL, Tykocki NR, Brayden JE, Hill-Eubanks D, Nelson MT. 2017. Capillary K^+-sensing initiates retrograde hyperpolarization to increase local cerebral blood flow. *Nature Neuroscience* **20**:717–726. DOI: https://doi.org/10.1038/nn.4533, PMID: 28319610

Longden TA, Nelson MT. 2015. Vascular inward rectifier K+ channels as external K+ sensors in the control of cerebral blood flow. *Microcirculation* **22**:183–196. DOI: https://doi.org/10.1111/micc.12190, PMID: 25641345

López AJ, Kramár E, Matheos DP, White AO, Kwapis J, Vogel-Ciernia A, Sakata K, Espinoza M, Wood MA. 2016. Promoter-Specific effects of DREADD modulation on hippocampal synaptic plasticity and memory formation. *Journal of Neuroscience* **36**:3588–3599. DOI: https://doi.org/10.1523/JNEUROSCI.3682-15.2016, PMID: 27013687

Lorthois S, Cassot F, Lauwers F. 2011. Simulation study of brain blood flow regulation by intra-cortical arterioles in an anatomically accurate large human vascular network. Part II: flow variations induced by global or localized modifications of arteriolar diameters. *NeuroImage* **54**:2840–2853. DOI: https://doi.org/10.1016/j.neuroimage.2010.10.040, PMID: 21047557

Maier A, Wilke M, Aura C, Zhu C, Ye FQ, Leopold DA. 2008. Divergence of fMRI and neural signals in V1 during perceptual suppression in the awake monkey. *Nature Neuroscience* **11**:1193–1200. DOI: https://doi.org/10.1038/nn.2173, PMID: 18711393

Marmarou A, Shulman K, LaMorgese J. 1975. Compartmental analysis of compliance and outflow resistance of the cerebrospinal fluid system. *Journal of Neurosurgery* **43**:523–534. DOI: https://doi.org/10.3171/jns.1975.43.5.0523, PMID: 1181384

Marmarou A, Shulman K, Rosende RM. 1978. A nonlinear analysis of the cerebrospinal fluid system and intracranial pressure dynamics. *Journal of Neurosurgery* **48**:332–344. DOI: https://doi.org/10.3171/jns.1978.48.3.0332, PMID: 632857

Mateo C, Knutsen PM, Tsai PS, Shih AY, Kleinfeld D. 2017. Entrainment of arteriole vasomotor fluctuations by neural activity is a basis of Blood-Oxygenation-Level-Dependent "Resting-State" Connectivity. *Neuron* **96**:936–948. DOI: https://doi.org/10.1016/j.neuron.2017.10.012, PMID: 29107517

Matthews EA, Schoch S, Dietrich D. 2013. Tuning local calcium availability: cell-type-specific immobile calcium buffer capacity in hippocampal neurons. *Journal of Neuroscience* **33**:14431–14445. DOI: https://doi.org/10.1523/JNEUROSCI.4118-12.2013, PMID: 24005295

McMahon SM, Jackson MB. 2018. An inconvenient truth: calcium sensors are calcium buffers. *Trends in Neurosciences* **41**:880–884. DOI: https://doi.org/10.1016/j.tins.2018.09.005, PMID: 30287084

Miettinen R, Sirviö J, Riekkinen P, Laakso MP, Riekkinen M, Riekkinen P. 1993. Neocortical, hippocampal and septal parvalbumin- and somatostatin-containing neurons in young and aged rats: correlation with passive avoidance and water maze performance. *Neuroscience* **53**:367–378. DOI: https://doi.org/10.1016/0306-4522(93)90201-P, PMID: 8098509

Mishra A, Reynolds JP, Chen Y, Gourine AV, Rusakov DA, Attwell D. 2016. Astrocytes mediate neurovascular signaling to capillary pericytes but not to arterioles. *Nature Neuroscience* **19**:1619–1627. DOI: https://doi.org/10.1038/nn.4428, PMID: 27775719

Moon CH, Fukuda M, Kim SG. 2013. Spatiotemporal characteristics and vascular sources of neural-specific and -nonspecific fMRI signals at submillimeter columnar resolution. *NeuroImage* **64**:91–103. DOI: https://doi.org/10.1016/j.neuroimage.2012.08.064, PMID: 22960251

Musall S, Kaufman MT, Juavinett AL, Gluf S, Churchland AK. 2019. Single-trial neural dynamics are dominated by richly varied movements. *Nature Neuroscience* **22**:1677–1686. DOI: https://doi.org/10.1038/s41593-019-0502-4, PMID: 31551604

Necchi D, Virgili M, Monti B, Contestabile A, Scherini E. 2002. Regional alterations of the NO/NOS system in the aging brain: a biochemical, histochemical and immunochemical study in the rat. *Brain Research* **933**:31–41. DOI: https://doi.org/10.1016/S0006-8993(02)02302-8, PMID: 11929633

Ngai AC, Winn HR. 1996. Estimation of shear and flow rates in pial arterioles during somatosensory stimulation. *The American Journal of Physiology* **270**:H1712–H1717. DOI: https://doi.org/10.1152/ajpheart.1996.270.5.H1712, PMID: 8928878

Nizar K, Uhlirova H, Tian P, Saisan PA, Cheng Q, Reznichenko L, Weldy KL, Steed TC, Sridhar VB, MacDonald CL, Cui J, Gratiy SL, Sakadžić S, Boas DA, Beka TI, Einevoll GT, Chen J, Masliah E, Dale AM, Silva GA, et al. 2013. In vivo stimulus-induced vasodilation occurs without IP3 receptor activation and may precede astrocytic calcium increase. *Journal of Neuroscience* **33**:8411–8422. DOI: https://doi.org/10.1523/JNEUROSCI.3285-12.2013, PMID: 23658179

Norwood JN, Zhang Q, Card D, Craine A, Ryan TM, Drew PJ. 2019. Anatomical basis and physiological role of cerebrospinal fluid transport through the murine cribriform plate. *eLife* **8**:e44278. DOI: https://doi.org/10.7554/eLife.44278, PMID: 31063132

O'Herron P, Chhatbar PY, Levy M, Shen Z, Schramm AE, Lu Z, Kara P. 2016. Neural correlates of single-vessel haemodynamic responses in vivo. *Nature* **534**:378–382. DOI: https://doi.org/10.1038/nature17965, PMID: 27281215

Okabe M, Ikawa M, Kominami K, Nakanishi T, Nishimune Y. 1997. 'Green mice' as a source of ubiquitous green cells. *FEBS Letters* **407**:313–319. DOI: https://doi.org/10.1016/S0014-5793(97)00313-X, PMID: 9175875

Otsu Y, Couchman K, Lyons DG, Collot M, Agarwal A, Mallet JM, Pfrieger FW, Bergles DE, Charpak S. 2015. Calcium dynamics in astrocyte processes during neurovascular coupling. *Nature Neuroscience* **18**:210–218. DOI: https://doi.org/10.1038/nn.3906, PMID: 25531572

Pachitariu M, Stringer C, Harris KD. 2018. Robustness of spike deconvolution for neuronal calcium imaging. *The Journal of Neuroscience* **38**:7976–7985. DOI: https://doi.org/10.1523/JNEUROSCI.3339-17.2018, PMID: 30082416

Parabucki A, Lampl I. 2017. Volume conduction coupling of Whisker-Evoked cortical LFP in the mouse olfactory bulb. *Cell Reports* **21**:919–925. DOI: https://doi.org/10.1016/j.celrep.2017.09.094, PMID: 29069599

Pati S, Salvi SS, Kallianpur M, Vaidya B, Banerjee A, Maiti S, Clement JP, Vaidya VA. 2019. Chemogenetic activation of excitatory neurons alters hippocampal neurotransmission in a Dose-Dependent manner. *Eneuro* **6**:ENEURO.0124-19.2019. DOI: https://doi.org/10.1523/ENEURO.0124-19.2019, PMID: 31645362

Perrenoud Q, Geoffroy H, Gauthier B, Rancillac A, Alfonsi F, Kessaris N, Rossier J, Vitalis T, Gallopin T. 2012. Characterization of type I and type II nNOS-Expressing interneurons in the barrel cortex of mouse. *Frontiers in Neural Circuits* **6**:36. DOI: https://doi.org/10.3389/fncir.2012.00036, PMID: 22754499

Pesaran B, Vinck M, Einevoll GT, Sirota A, Fries P, Siegel M, Truccolo W, Schroeder CE, Srinivasan R. 2018. Investigating large-scale brain dynamics using field potential recordings: analysis and interpretation. *Nature Neuroscience* **21**:903–919. DOI: https://doi.org/10.1038/s41593-018-0171-8, PMID: 29942039

Phillips EA, Hasenstaub AR. 2016. Asymmetric effects of activating and inactivating cortical interneurons. *eLife* **5**:e18383. DOI: https://doi.org/10.7554/eLife.18383, PMID: 27719761

Pigott B, Bartus K, Garthwaite J. 2013. On the selectivity of neuronal NOS inhibitors. *British Journal of Pharmacology* **168**:1255–1265. DOI: https://doi.org/10.1111/bph.12016, PMID: 23072468

Pisanello M, Pisano F, Hyun M, Maglie E, Balena A, De Vittorio M, Sabatini BL, Pisanello F. 2019. The Three-Dimensional signal collection field for fiber photometry in brain tissue. *Frontiers in Neuroscience* **13**:82. DOI: https://doi.org/10.3389/fnins.2019.00082, PMID: 30863275

Poulos TL, Li H. 2017. Nitric oxide synthase and structure-based inhibitor design. *Nitric Oxide* **63**:68–77. DOI: https://doi.org/10.1016/j.niox.2016.11.004, PMID: 27890696

Reiner A, Zagvazdin Y. 1998. On the selectivity of 7-nitroindazole as an inhibitor of neuronal nitric oxide synthase. *Trends in Pharmacological Sciences* **19**:348–350. DOI: https://doi.org/10.1016/S0165-6147(98)01194-8, PMID: 9786021

Roggendorf W, Cervós-Navarro J. 1977. Ultrastructure of arterioles in the cat brain. *Cell and Tissue Research* **178**:495–515. DOI: https://doi.org/10.1007/BF00219571, PMID: 870204

Ruitenberg A, den Heijer T, Bakker SL, van Swieten JC, Koudstaal PJ, Hofman A, Breteler MM. 2005. Cerebral hypoperfusion and clinical onset of dementia: the rotterdam study. *Annals of Neurology* **57**:789–794. DOI: https://doi.org/10.1002/ana.20493, PMID: 15929050

Rungta RL, Chaigneau E, Osmanski BF, Charpak S. 2018. Vascular compartmentalization of functional hyperemia from the synapse to the pia. *Neuron* **99**:362–375. DOI: https://doi.org/10.1016/j.neuron.2018.06.012, PMID: 29937277

Sabbagh MF, Heng JS, Luo C, Castanon RG, Nery JR, Rattner A, Goff LA, Ecker JR, Nathans J. 2018. Transcriptional and epigenomic landscapes of CNS and non-CNS vascular endothelial cells. *eLife* **7**:e36187. DOI: https://doi.org/10.7554/eLife.36187, PMID: 30188322

Salkoff DB, Zagha E, McCarthy E, McCormick DA. 2020. Movement and performance explain widespread cortical activity in a visual detection task. *Cerebral Cortex* **30**:421–437. DOI: https://doi.org/10.1093/cercor/bhz206, PMID: 31711133

Saloman JL, Scheff NN, Snyder LM, Ross SE, Davis BM, Gold MS. 2016. Gi-DREADD expression in peripheral nerves produces Ligand-Dependent analgesia, as well as Ligand-Independent functional changes in sensory neurons. *The Journal of Neuroscience* **36**:10769–10781. DOI: https://doi.org/10.1523/JNEUROSCI.3480-15.2016, PMID: 27798132

Schmid F, Tsai PS, Kleinfeld D, Jenny P, Weber B. 2017. Depth-dependent flow and pressure characteristics in cortical microvascular networks. *PLOS Computational Biology* **13**:e1005392. DOI: https://doi.org/10.1371/journal.pcbi.1005392, PMID: 28196095

Schram G, Pourrier M, Wang Z, White M, Nattel S. 2003. Barium block of Kir2 and human cardiac inward rectifier currents: evidence for subunit-heteromeric contribution to native currents. *Cardiovascular Research* **59**:328–338. DOI: https://doi.org/10.1016/S0008-6363(03)00366-3, PMID: 12909316

Schulz K, Sydekum E, Krueppel R, Engelbrecht CJ, Schlegel F, Schröter A, Rudin M, Helmchen F. 2012. Simultaneous BOLD fMRI and fiber-optic calcium recording in rat neocortex. *Nature Methods* **9**:597–602. DOI: https://doi.org/10.1038/nmeth.2013, PMID: 22561989

Segal SS. 2000. Integration of blood flow control to skeletal muscle: key role of feed arteries. *Acta Physiologica Scandinavica* **168**:511–518. DOI: https://doi.org/10.1046/j.1365-201x.2000.00703.x, PMID: 10759588

Segal SS. 2005. Regulation of blood flow in the microcirculation. *Microcirculation* **12**:33–45. DOI: https://doi.org/10.1080/10739680590895028, PMID: 15804972

Shih AY, Friedman B, Drew PJ, Tsai PS, Lyden PD, Kleinfeld D. 2009a. Active dilation of penetrating arterioles restores red blood cell flux to penumbral neocortex after focal stroke. *Journal of Cerebral Blood Flow & Metabolism* **29**:738–751. DOI: https://doi.org/10.1038/jcbfm.2008.166, PMID: 19174826

Shih YY, Chen CC, Shyu BC, Lin ZJ, Chiang YC, Jaw FS, Chen YY, Chang C. 2009b. A new scenario for negative functional magnetic resonance imaging signals: endogenous neurotransmission. *Journal of Neuroscience* **29**:3036–3044. DOI: https://doi.org/10.1523/JNEUROSCI.3447-08.2009, PMID: 19279240

Shih YY, Wey HY, De La Garza BH, Duong TQ. 2011. Striatal and cortical BOLD, blood flow, blood volume, oxygen consumption, and glucose consumption changes in noxious forepaw electrical stimulation. *Journal of Cerebral Blood Flow & Metabolism* **31**:832–841. DOI: https://doi.org/10.1038/jcbfm.2010.173, PMID: 20940730

Shih AY, Mateo C, Drew PJ, Tsai PS, Kleinfeld D. 2012a. A polished and reinforced Thinned-skull window for Long-term imaging of the mouse brain. *Journal of Visualized Experiments* **1**:3742. DOI: https://doi.org/10.3791/3742

Shih AY, Driscoll JD, Drew PJ, Nishimura N, Schaffer CB, Kleinfeld D. 2012b. Two-photon microscopy as a tool to study blood flow and neurovascular coupling in the rodent brain. *Journal of Cerebral Blood Flow & Metabolism* **32**:1277–1309. DOI: https://doi.org/10.1038/jcbfm.2011.196, PMID: 22293983

Sirotin YB, Das A. 2009. Anticipatory haemodynamic signals in sensory cortex not predicted by local neuronal activity. *Nature* **457**:475–479. DOI: https://doi.org/10.1038/nature07664, PMID: 19158795

Steelman SM, Wu Q, Wagner HP, Yeh AT, Humphrey JD. 2010. Perivascular tethering modulates the geometry and biomechanics of cerebral arterioles. *Journal of Biomechanics* **43**:2717–2721. DOI: https://doi.org/10.1016/j.jbiomech.2010.06.024, PMID: 20655047

Stefanovic B, Schwindt W, Hoehn M, Silva AC. 2007. Functional uncoupling of hemodynamic from neuronal response by inhibition of neuronal nitric oxide synthase. *Journal of Cerebral Blood Flow & Metabolism* **27**:741–754. DOI: https://doi.org/10.1038/sj.jcbfm.9600377, PMID: 16883353

Stringer C, Pachitariu M, Steinmetz N, Reddy CB, Carandini M, Harris KD. 2019. Spontaneous behaviors drive multidimensional, brainwide activity. *Science* **364**:255. DOI: https://doi.org/10.1126/science.aav7893, PMID: 31000656

Tanaka K, Gotoh F, Gomi S, Takashima S, Mihara B, Shirai T, Nogawa S, Nagata E. 1991. Inhibition of nitric oxide synthesis induces a significant reduction in local cerebral blood flow in the rat. *Neuroscience Letters* **127**:129–132. DOI: https://doi.org/10.1016/0304-3940(91)90911-C, PMID: 1881609

Tasic B, Menon V, Nguyen TN, Kim TK, Jarsky T, Yao Z, Levi B, Gray LT, Sorensen SA, Dolbeare T, Bertagnolli D, Goldy J, Shapovalova N, Parry S, Lee C, Smith K, Bernard A, Madisen L, Sunkin SM, Hawrylycz M, et al. 2016.

Adult mouse cortical cell taxonomy revealed by single cell transcriptomics. *Nature Neuroscience* **19**:335–346. DOI: https://doi.org/10.1038/nn.4216, PMID: 26727548

Theis L, Berens P, Froudarakis E, Reimer J, Román Rosón M, Baden T, Euler T, Tolias AS, Bethge M. 2016. Benchmarking spike rate inference in population calcium imaging. *Neuron* **90**:471–482. DOI: https://doi.org/10.1016/j.neuron.2016.04.014, PMID: 27151639

Tian P, Teng IC, May LD, Kurz R, Lu K, Scadeng M, Hillman EM, De Crespigny AJ, D'Arceuil HE, Mandeville JB, Marota JJ, Rosen BR, Liu TT, Boas DA, Buxton RB, Dale AM, Devor A. 2010. Cortical depth-specific microvascular dilation underlies laminar differences in blood oxygenation level-dependent functional MRI signal. *PNAS* **107**:15246–15251. DOI: https://doi.org/10.1073/pnas.1006735107, PMID: 20696904

Tomioka R, Okamoto K, Furuta T, Fujiyama F, Iwasato T, Yanagawa Y, Obata K, Kaneko T, Tamamaki N. 2005. Demonstration of long-range GABAergic connections distributed throughout the mouse neocortex. *European Journal of Neuroscience* **21**:1587–1600. DOI: https://doi.org/10.1111/j.1460-9568.2005.03989.x, PMID: 15845086

Tomioka R, Rockland KS. 2007. Long-distance corticocortical GABAergic neurons in the adult monkey white and gray matter. *The Journal of Comparative Neurology* **505**:526–538. DOI: https://doi.org/10.1002/cne.21504, PMID: 17924571

Tran CHT, Peringod G, Gordon GR. 2018. Astrocytes integrate behavioral state and vascular signals during functional hyperemia. *Neuron* **100**:1133–1148. DOI: https://doi.org/10.1016/j.neuron.2018.09.045, PMID: 30482689

Uhlirova H, Kılıç K, Tian P, Sakadžić S, Gagnon L, Thunemann M, Desjardins M, Saisan PA, Nizar K, Yaseen MA, Hagler DJ, Vandenberghe M, Djurovic S, Andreassen OA, Silva GA, Masliah E, Kleinfeld D, Vinogradov S, Buxton RB, Einevoll GT, et al. 2016a. The roadmap for estimation of cell-type-specific neuronal activity from non-invasive measurements. *Philosophical Transactions of the Royal Society B: Biological Sciences* **371**: 20150356. DOI: https://doi.org/10.1098/rstb.2015.0356, PMID: 27574309

Uhlirova H, Kılıç K, Tian P, Thunemann M, Desjardins M, Saisan PA, Sakadžić S, Ness TV, Mateo C, Cheng Q, Weldy KL, Razoux F, Vandenberghe M, Cremonesi JA, Ferri CG, Nizar K, Sridhar VB, Steed TC, Abashin M, Fainman Y, et al. 2016b. Cell type specificity of neurovascular coupling in cerebral cortex. *eLife* **5**:e14315. DOI: https://doi.org/10.7554/eLife.14315, PMID: 27244241

Urban DJ, Roth BL. 2015. DREADDs (designer receptors exclusively activated by designer drugs): chemogenetic tools with therapeutic utility. *Annual Review of Pharmacology and Toxicology* **55**:399–417. DOI: https://doi.org/10.1146/annurev-pharmtox-010814-124803, PMID: 25292433

Valtschanoff JG, Weinberg RJ, Kharazia VN, Schmidt HH, Nakane M, Rustioni A. 1993. Neurons in rat cerebral cortex that synthesize nitric oxide: nadph diaphorase histochemistry, NOS Immunocytochemistry, and colocalization with GABA. *Neuroscience Letters* **157**:157–161. DOI: https://doi.org/10.1016/0304-3940(93)90726-2, PMID: 7694193

Vanlandewijck M, He L, Mäe MA, Andrae J, Ando K, Del Gaudio F, Nahar K, Lebouvier T, Laviña B, Gouveia L, Sun Y, Raschperger E, Räsänen M, Zarb Y, Mochizuki N, Keller A, Lendahl U, Betsholtz C. 2018. A molecular atlas of cell types and zonation in the brain vasculature. *Nature* **554**:475–480. DOI: https://doi.org/10.1038/nature25739, PMID: 29443965

Vazquez AL, Fukuda M, Crowley JC, Kim SG. 2014. Neural and hemodynamic responses elicited by forelimb- and photo-stimulation in channelrhodopsin-2 mice: insights into the hemodynamic point spread function. *Cerebral Cortex* **24**:2908–2919. DOI: https://doi.org/10.1093/cercor/bht147, PMID: 23761666

Vazquez AL, Fukuda M, Kim SG. 2018. Inhibitory neuron activity contributions to hemodynamic responses and metabolic load examined using an inhibitory optogenetic mouse model. *Cerebral Cortex* **28**:4105–4119. DOI: https://doi.org/10.1093/cercor/bhy225, PMID: 30215693

Vruwink M, Schmidt HH, Weinberg RJ, Burette A. 2001. Substance P and nitric oxide signaling in cerebral cortex: anatomical evidence for reciprocal signaling between two classes of interneurons. *The Journal of Comparative Neurology* **441**:288–301. DOI: https://doi.org/10.1002/cne.1413, PMID: 11745651

Weickenmeier J, Kurt M, Ozkaya E, Wintermark M, Pauly KB, Kuhl E. 2018a. Magnetic resonance elastography of the brain: a comparison between pigs and humans. *Journal of the Mechanical Behavior of Biomedical Materials* **77**:702–710. DOI: https://doi.org/10.1016/j.jmbbm.2017.08.029, PMID: 28919161

Weickenmeier J, Kurt M, Ozkaya E, de Rooij R, Ovaert TC, Ehman RL, Butts Pauly K, Kuhl E. 2018b. Brain stiffens post mortem. *Journal of the Mechanical Behavior of Biomedical Materials* **84**:88–98. DOI: https://doi.org/10.1016/j.jmbbm.2018.04.009, PMID: 29754046

Welsh DG, Tran CHT, Hald BO, Sancho M. 2018. The conducted vasomotor response: function, biophysical basis, and pharmacological control. *Annual Review of Pharmacology and Toxicology* **58**:391–410. DOI: https://doi.org/10.1146/annurev-pharmtox-010617-052623, PMID: 28968190

Whittaker JR, Driver ID, Bright MG, Murphy K. 2016. The absolute CBF response to activation is preserved during elevated perfusion: implications for neurovascular coupling measures. *NeuroImage* **125**:198–207. DOI: https://doi.org/10.1016/j.neuroimage.2015.10.023, PMID: 26477657

Williams RH, Vazquez-DeRose J, Thomas AM, Piquet J, Cauli B, Kilduff TS. 2018. Cortical nNOS/NK1 receptor neurons are regulated by cholinergic projections from the basal forebrain. *Cerebral Cortex* **28**:1959–1979. DOI: https://doi.org/10.1093/cercor/bhx102, PMID: 28472227

Williams RH, Black SW, Thomas AM, Piquet J, Cauli B, Kilduff TS. 2019. Excitation of cortical nNOS/NK1R neurons by hypocretin 1 is independent of sleep homeostasis. *Cerebral Cortex* **29**:1090–1108. DOI: https://doi.org/10.1093/cercor/bhy015, PMID: 29462275

Winder AT, Echagarruga C, Zhang Q, Drew PJ. 2017. Weak correlations between hemodynamic signals and ongoing neural activity during the resting state. *Nature Neuroscience* **20**:1761–1769. DOI: https://doi.org/10.1038/s41593-017-0007-y, PMID: 29184204

Wölfle SE, Chaston DJ, Goto K, Sandow SL, Edwards FR, Hill CE. 2011. Non-linear relationship between hyperpolarisation and relaxation enables long distance propagation of vasodilatation. *The Journal of Physiology* **589**:2607–2623. DOI: https://doi.org/10.1113/jphysiol.2010.202580, PMID: 21486765

Wolters FJ, Zonneveld HI, Hofman A, van der Lugt A, Koudstaal PJ, Vernooij MW, Ikram MA, Heart-Brain Connection Collaborative Research Group. 2017. Cerebral perfusion and the risk of dementia: a Population-Based study. *Circulation* **136**:719–728. DOI: https://doi.org/10.1161/CIRCULATIONAHA.117.027448, PMID: 28588075

Yousef T, Neubacher U, Eysel UT, Volgushev M. 2004. Nitric oxide synthase in rat visual cortex: an immunohistochemical study. *Brain Research Protocols* **13**:57–67. DOI: https://doi.org/10.1016/j.brainresprot.2004.01.004, PMID: 15063842

Yuan P, Grutzendler J. 2016. Attenuation of β-Amyloid deposition and neurotoxicity by chemogenetic modulation of neural activity. *The Journal of Neuroscience* **36**:632–641. DOI: https://doi.org/10.1523/JNEUROSCI.2531-15.2016, PMID: 26758850

Zeisel A, Hochgerner H, Lönnerberg P, Johnsson A, Memic F, van der Zwan J, Häring M, Braun E, Borm LE, La Manno G, Codeluppi S, Furlan A, Lee K, Skene N, Harris KD, Hjerling-Leffler J, Arenas E, Ernfors P, Marklund U, Linnarsson S. 2018. Molecular architecture of the mouse nervous system. *Cell* **174**:999–1014. DOI: https://doi.org/10.1016/j.cell.2018.06.021, PMID: 30096314

Zhang Q, Roche M, Gheres KW, Chaigneau E, Kedarasetti RT, Haselden WD, Charpak S, Drew PJ. 2019. Cerebral oxygenation during locomotion is modulated by respiration. *Nature Communications* **10**:5515. DOI: https://doi.org/10.1038/s41467-019-13523-5, PMID: 31797933